# SUPPORTING INFORMATION

# Making soluble $Dy_2$ single-molecule magnets red emissive through their functionalization by ruthenium–cyanido luminophores

Michal Liberka[a,b] and Szymon Chorazy*[,a]

[a]Faculty of Chemistry, Jagiellonian University, Gronostajowa 2, 30-387 Krakow, Poland
[b]Doctoral School of Exact and Natural Sciences, Jagiellonian University, Lojasiewicza 11, 30-348 Krakow, Poland
*Corresponding author: simon.chorazy@uj.edu.pl

## Experimental section

## Materials

All commercially available reagents used for syntheses of precursors and presented compounds, including $RuCl_3 3H_2O$ (Sigma Aldrich, 95 %; CAS 14898-67-0), 1,10-phenanthroline (phen; Sigma Aldrich, 99 %; CAS 66–71–7), NaCN (Sigma Aldrich, 96 %; CAS 143-33-9), LiCl (Sigma Aldrich, 99 %; CAS 7447-41-8), $Dy^{III}(CF_3SO_3)_3$ (Sigma Aldrich, 99.99 %; CAS 139177-62-1), 4-pyridone (4-pyone; Sigma Aldrich, 95 %; CAS 108-96-3), and all necessary solvents, were used as received without further purification.

## Synthesis and basic physicochemical characterization

### Synthesis of cis-[Ru$^{II}$(CN)$_2$(phen)$_2$]·2H$_2$O precursor

The ruthenium(II)–cyanido precursor was prepared by modifications of literature procedures.[S1–S2] Firstly, the cis-[Ru$^{II}$(Cl)$_2$(phen)$_2$] precursor was obtained by refluxing the Ru$^{III}$Cl$_3$3H$_2$O (1.5 g, 5.74 mmol), 1,10-phenanthroline (2.1 g, 11.7 mmol), and LiCl (1.6 g, 0.04 mmol) in dimethylformamide (12 mL) for 8 h. To the resulting solution, the 50 mL portion of acetone was added, and the mixture was cooled at 0°C overnight. The precipitated solid was filtered, washed with water and diethyl ether, and dried in the air (yield: 1.5 g, 50 %, based on Ru).[S1] In the second step, the 95.4 mg portion (1.95 mmol) of NaCN dissolved in the 25 ml portion of water was poured into the 100 ml of the ethanol solution of cis-[Ru$^{II}$(Cl)$_2$(phen)$_2$] precursor (0.5 g, 0.94 mmol), and the mixture was refluxed for 2 days. After this time, the solution was filtered and evaporated to dryness at room temperature. The residue was dissolved in 10 mL of ethanol, filtered off, and evaporated. This step was repeated three times to give a reddish crude solid. Finally, the obtained product was recrystallized from boiling water to give a reddish microcrystalline solid (yield: 0.4 g, 77 %, based on Ru).[S2] The complex was chromatographically pure as shown by using silica gel and methanol. The formula of the obtained air-stable precursor, cis-[Ru$^{II}$(CN)$_2$(phen)$_2$]·2H$_2$O, was determined by the CHN elemental analysis and thermogravimetric (TG) measurements (Fig. S2), supported by infrared absorption (IR) spectroscopy (Fig. S3). CHN elemental analysis. Anal. Calcd. for $C_{26}H_{20}N_6O_2Ru_1$ ($M_W$ = 549.5 g·mol$^{-1}$): C, 56.82 %; H, 3.67 %; N, 15.29 %. Found: C, 57.11 %; H, 3.31 %; N, 15.36 %. TG (Fig. S1). Loss of 2 H$_2$O molecules per the [Ru$^{II}$(CN)$_2$(phen)$_2$] complex, calcd.: 6.56 %; found: 6.63 %. IR spectrum (Fig. S2, KBr). C≡N$^-$ stretching vibrations: 2069 cm$^{-1}$, indicating the presence of only terminal cyanido ligand modes. A broader analysis of other peaks of IR spectra can be found in the comment placed below Fig. S3.

### Syntheses of Dy$_2$Ru$_2$, Dy$_2$Fe$_{1.2}$Ru$_{0.8}$, and Dy$_2$Fe$_{0.8}$Ru$_{1.2}$

The main compound, **Dy$_2$Ru$_2$**, was prepared by the modification of the procedure described by us for the iron(II) analog.[S3] The 0.025 mmol (13.7 mg) portion of cis-[Ru$^{II}$(CN)$_2$(phen)$_2$]·2H$_2$O, and the 0.025 mmol (15.2 mg) portion of Dy$^{III}$(CF$_3$SO$_3$)$_3$ were dissolved together in 3 mL of a MeOH-MeCN (1:1, v/v) mixture. After mixing for ca. 1 min, the freshly prepared solution of 4-pyone ligand (0.50 mmol, 47.6 mg) in the 2 mL of a MeOH-MeCN (1:1, v/v) mixed solvent was added. The resulting solution was stirred for ca. 10 min, then filtered, and, diethyl ether was carefully layered on the top of the resulting solution. After about a few days, a large number of small red block crystals of **Dy$_2$Ru$_2$** appeared. Their crystal structure, in contrast to the iron(II) **Dy$_2$Fe$_2$** analog,[S3] could not be determined by single-crystal X-ray diffraction. The formula of **Dy$_2$Ru$_2$**, {[Dy$^{III}$(4-pyone)$_5$]$_2$[Ru$^{II}$(CN)$_2$(phen)$_2$]$_2$}·(CF$_3$SO$_3$)$_6$·2MeOH ($M_W$ = 3261.5 g·mol$^{-1}$), was deduced by the structural analogy with **Dy$_2$Fe$_2$**, as indicated by the mass spectroscopy (MS, Fig. S1) and powder X-ray diffraction method (P-XRD, Fig. S5), which were supported by IR absorption spectroscopy (Fig. S3), confronted with the results of TGA measurements (Fig. S2). All these measurements confirmed that the obtained **Dy$_2$Ru$_2$** is isostructural with previously reported **Dy$_2$Fe$_2$** sharing the identical formula differing only in the type of metal in the cyanido complex.

Moreover, according to the above procedure, we synthesized two additional compounds with the Fe(II)–Ru(II) mixture on the cyanido-metal-complex side, namely **Dy$_2$Fe$_{1.2}$Ru$_{0.8}$** and **Dy$_2$Fe$_{0.8}$Ru$_{1.2}$** with lower ruthenium content. They were synthesized using appropriate mixtures of [Fe$^{II}$(CN)$_2$(phen)$_2$]·2H$_2$O and [Ru$^{II}$(CN)$_2$(phen)$_2$]·2H$_2$O complexes, where the molar ratio Fe:Re was set to be 3:2 and 2:3 in **Dy$_2$Fe$_{1.2}$Ru$_{0.8}$** and **Dy$_2$Fe$_{0.8}$Ru$_{1.2}$**, respectively, targeting the expected composition of the resultant solid-state phases, according to the protocol used recently

for the solid solutions.[S4–S5] That allowed us to obtain crystals that were suitable for single-crystal X-ray diffraction studies, which support the above deductions concerning the crystal structure of **Dy$_2$Ru$_2$** (for more information see the crystal structure determination below). Their composition of {[Dy$^{III}$(4-pyone)$_5$]$_2$[Fe$^{II}_x$Ru$^{II}_{2-x}$(CN)$_2$(phen)$_2$]$_2$}·(CF$_3$SO$_3$)$_6$·2MeOH ($x$ = 1.2 in **Dy$_2$Fe$_{1.2}$Ru$_{0.8}$** and 0.8 in **Dy$_2$Fe$_{0.8}$Ru$_{1.2}$**, $M_W$ = 3207.3 and 3225.4 g·mol$^{-1}$, respectively), was determined by a single-crystal X-ray diffraction (SC-XRD) analysis, while the phase purity was proven by powder X-ray diffraction method (Fig. S5), supported by the results of CHNS elemental analysis and IR spectroscopy. The exact molar fractions of Fe$^{2+}$ and Ru$^{2+}$ ions were determined by the energy dispersive X-ray microanalysis (SEM-EDXMA, Table S1) and mass spectroscopy (MS, Fig. S1 and Table S2).

Basic characterization of **Dy$_2$Ru$_2$**. EDXMA (Table S1). Found atomic composition (normalized for 2 Dy centers): Ru, 1.97. MS spectroscopy (Fig. S1). Found relative atomic composition: Ru, 1.99. CHNS elem. analysis. Calcd. for C$_{110}$H$_{90}$Dy$_2$F$_{18}$Ru$_2$N$_{22}$O$_{30}$S$_6$: C, 40.51 %; H, 2.78 %; N, 9.45 %; S, 5.90 %. Found: C, 40.63 %; H, 2.61 %; N, 9.58 %; S, 5.77. TG (Fig. S2). Loss of 2 MeOH molecules per the {Dy$_2$Ru$_2$} unit, calcd.: 1.96 %; found: 2.01 %. IR spectrum (Fig. S3, KBr). C≡N$^-$ stretching vibrations: 2105, 2190, and 2076 cm$^{-1}$, indicating the presence of both bridging and terminal cyanido ligand modes.

Basic characterization of **Dy$_2$Fe$_{0.8}$Ru$_{1.2}$**. EDXMA (Table S1). Found atomic composition (normalized for 2 Dy centers): Fe, 0.82; Ru, 1.18. MS spectroscopy (Fig. S1). Found relative atomic composition: Fe, 0.83; Ru, 1.17. CHNS elem. analysis. Calcd. for C$_{110}$H$_{90}$Dy$_2$F$_{18}$Fe$_{0.8}$Ru$_{1.2}$N$_{22}$O$_{30}$S$_6$: C, 40.96 %; H, 2.81 %; N, 9.55 %; S, 5.97 %. Found: C, 41.07 %; H, 2.78 %; N, 9.47 %; S, 6.07 %. TG (Fig. S2). Loss of 2 MeOH molecules per the {Dy$_2$Fe$_{0.8}$Ru$_{1.2}$} unit, calcd.: 1.99 %; found: 1.95 %. IR spectrum (Fig. S3, KBr). C≡N$^-$ stretching vibrations: 2106, 2187, and 2076 cm$^{-1}$, indicating the presence of both bridging and terminal cyanido ligand modes.

Basic characterization of **Dy$_2$Fe$_{1.2}$Ru$_{0.8}$**. EDXMA (Table S1). Found atomic composition (normalized for 2 Dy centers): Fe, 1.16; Ru, 0.81. MS spectroscopy (Fig. S1). Found relative atomic composition: Fe, 1.16; Ru, 0.84. CHNS elem. analysis. Calcd. for C$_{110}$H$_{90}$Dy$_2$F$_{18}$Fe$_{1.2}$Ru$_{0.8}$N$_{22}$O$_{30}$S$_6$: C, 41.19 %; H, 2.83 %; N, 9.61 %; S, 6.00 %. Found: C, 40.99 %; H, 2.68 %; N, 9.84 %; S, 5.89 %. TG (Fig. S2). Loss of 2 MeOH molecules per the {Dy$_2$Fe$_{1.2}$Ru$_{0.8}$} unit, calcd.: 2.00 %; found: 1.98 %. IR spectrum (Fig. S3, KBr). C≡N$^-$ stretching vibrations: 2108, 2194, and 2077 cm$^{-1}$, indicating the presence of both bridging and terminal cyanido ligand modes.

## X-ray crystallography

The single-crystal X-ray diffraction (SC-XRD) data for **Dy$_2$Fe$_{1.2}$Ru$_{0.8}$** and **Dy$_2$Fe$_{0.8}$Ru$_{1.2}$** were collected using a Bruker D8 Quest diffractometer equipped with a Photon50 CMOS detector, MoK$\alpha$ (0.71073 Å) irradiation source, a graphite monochromator, and an Oxford Cryostream cooling system. The single crystals were mounted on Micro MountsTM and measured at 100(2) K. The SAINT and SADABS programs were employed for data reduction and cell refinement processes. The absorption correction was executed using the TWINABS program.[S6] The crystal structures were solved by an intrinsic phasing method using a SHELXT program within the Apex3 package,[S7] and then refined by a weighted full-matrix least-squares method on $F^2$ of SHELX-2014/7 within the WinGX (ver. 2014.1) software.[S8] All non-hydrogen atoms were refined with anisotropic displacement parameters, while the positions of hydrogen atoms in 1,10-phenanthroline and 4-pyridone ligands as well as solvent molecules were assigned at the idealized positions and refined using a riding model. The crystal structure of **Dy$_2$Fe$_{1.2}$Ru$_{0.8}$** follows a good structural order as in **Dy$_2$Fe$_2$**,[S3] so only a few small structural restraints on crystallization solvent molecules and triflate anions were applied to ensure the proper geometry and the convergence of the refinement process. On the other hand, in the crystal structure with a predominance of ruthenium, **Dy$_2$Fe$_{0.8}$Ru$_{1.2}$**, a few equivalent positions of 4-pyone ligands as well as solvent molecules and anions were found (Fig. S4). Therefore, using a significant amount of ISOR and DFIX restraints, only the two largest components of disordered ligands were modeled (ses Fig. S4). Such a structural disorder was reproducible for several measured crystals, which suggests that larger Ru(II) centers in the structure cause the increased disorder and more possibilities for the 4-pyone ligand organization at Dy(III) centers. This might explain why satisfactory crystalline data for **Dy$_2$Ru$_2$** could not be obtained. Despite the above-mentioned disorder, satisfactory refinement parameters were achieved both for **Dy$_2$Fe$_{1.2}$Ru$_{0.8}$** and **Dy$_2$Fe$_{0.8}$Ru$_{1.2}$**. Full details of crystal data and structure refinement parameters for **Dy$_2$Fe$_{1.2}$Ru$_{0.8}$** and **Dy$_2$Fe$_{0.8}$Ru$_{1.2}$** are gathered in Table S3. Detailed structure parameters can be found in Table S4, while the

representative structural views, prepared using the Mercury 2022.1.0 software, are presented in Fig. S3. CCDC reference numbers for the crystal structures of **Dy$_2$Fe$_{1.2}$Ru$_{0.8}$** and **Dy$_2$Fe$_{0.8}$Ru$_{1.2}$** are 2375974 and 2375975, respectively.

The purity and phase uniformity were checked by powder X-ray diffraction (P-XRD) experiments, measured at room temperature using Bruker D8 Advance Eco powder diffractometer equipped with a CuK$\alpha$ (1.5419 Å) radiation source and capillary spinning add-on (Fig. S5). The NTREOR09 program with the EXPO system was used for the identification and Miller indexing of all of the observed maxima in **Dy$_2$Fe$_{1.2}$Ru$_{0.8}$**, **Dy$_2$Fe$_{0.8}$Ru$_{1.2}$**, and **Dy$_2$Ru$_2$** (Fig. S5, Table S6).[S9,S10]

**Physical techniques**

Elemental analyses of CHNS were performed on an Elemental Vario Micro Cube CHNS analyzer while those of metals were conducted using a Hitachi S-4700 SEM microscope equipped with a NORAN VINTAGE energy dispersive X-ray microanalysis system. The mass spectra were measured using a high-resolution tandem time-of-flight mass spectrometer with electrospray ionization (ESI-QTOF) at a flow of 180 µL/h in positive and negative ionization mode in the scanning range 50–1300 m/z. The TGA curves were collected under a nitrogen atmosphere using a NETZSCH TG209 F1 Libra thermogravimetric analyzer with Al pans as holders in the 20–370°C temperature range. Infrared (IR) absorption spectra were measured on selected crystals using a Thermo Scientific Nicolet iN10 FTIR spectrometer in the range 4000–700 cm$^{-1}$. The UV-vis absorption spectra were collected using a Shimadzu UV-3600 spectrophotometer in the range of 300–800 nm.

Investigation of magnetic properties was performed using a Quantum Design MPMS-3 Evercool magnetometer. For magnetic studies, the powder sample was placed in the glass tube, covered by a small amount of diethyl ether. Diamagnetic corrections from the sample, the Et$_2$O solvent, and the sample holder were taken into account. The detailed analysis of *ac* magnetic data, including the determination of magnetic relaxation times from the simultaneous fitting of all *ac* magnetic characteristics (frequency dependences of out-of-phase and in-phase magnetic susceptibilities together with the related Argand plots) using models for complex-valued *ac* susceptibility at the indicated conditions of *dc* magnetic field and temperature as well as further determination of final parameters of operating relaxation processes from the simultaneous 3D fitting of temperature- and field-dependences of relaxation times, was performed using the *relACs* program (see more details on the fitting procedures in the comment to Fig. S6–S8 and Table S7).[S11]

The photoluminescent characteristics including emission and excitation spectra were measured using an FS5 spectrofluorometer equipped with an Xe (150 W) arc lamp as an excitation source and a Hamamatsu photomultiplier of the R928P type as an emission detector. Emission lifetime measurements were conducted on the FS5 spectrofluorometer using an FS5 multichannel scaling module with a microsecond Xe flash lamp (5 W). Absolute luminescence quantum yields were determined by a direct excitation method using an integrating sphere module for the FS5 spectrofluorometer using barium sulfate as the reference material.[S12] Luminescent background corrections were performed within the Fluoracle software.

Continuous Shape Measure (CShM) analyses for determination of the coordination geometry of Dy$^{III}$ and Fe$^{II}$/Ru$^{II}$ complexes were conducted using the SHAPE software, version 2.1.[S13–S14]

**Table S1** Results of energy dispersive X-ray microanalysis on SEM (SEM-EDXMA) of selected atom composition in **Dy$_2$Fe$_2$**,[S3] **Dy$_2$Fe$_{1.2}$Ru$_{0.8}$**, **Dy$_2$Fe$_{0.8}$Ru$_{1.2}$**, and **Dy$_2$Ru$_2$**.

| atom | S | Dy | Fe | Ru |
|---|---|---|---|---|
| compound **Dy$_2$Fe$_2$** (measured as a reference)[S3] | | | | |
| measured atomic composition (only selected atom included, independent measurements) / % | 35.23 ($\pm$0.71) | 11.97 ($\pm$0.73) | 12.00 ($\pm$0.65) | – |
| | 34.38 ($\pm$0.80) | 12.86 ($\pm$0.59) | 12.38 ($\pm$0.98) | – |
| | 32.76 ($\pm$0.47) | 10.16 ($\pm$0.49) | 11.34 ($\pm$0.60) | – |
| | 34.38 ($\pm$0.37) | 9.27 ($\pm$0.38) | 11.91 ($\pm$0.34) | – |
| | 32.38 ($\pm$0.37) | 12.27 ($\pm$0.38) | 10.98 ($\pm$0.34) | – |
| | 33.45 ($\pm$0.38) | 13.19 ($\pm$0.40) | 9.89 ($\pm$0.49) | – |
| | 37.09 ($\pm$0.37) | 9.94 ($\pm$0.39) | 11.01 ($\pm$0.35) | – |
| | 34.42 ($\pm$0.81) | 12.83 ($\pm$0.55) | 11.52 ($\pm$0.67) | – |
| average atomic composition (only metals included) / % | 34.26 ($\pm$0.54) | 11.56 ($\pm$0.49) | 11.38 ($\pm$0.55) | – |
| relative atomic composition (only metals included, calculated for 2 Dy centers) | 5.93 ($\pm$0.09) | 2 | 1.97 ($\pm$0.10) | – |
| proposed metal composition | **6** | **2** | **2** | – |
| compound **Dy$_2$Fe$_{1.2}$Ru$_{0.8}$** | | | | |
| measured atomic composition (only selected atom included, independent measurements) / % | 36.41 ($\pm$0.74) | 12.00 ($\pm$0.69) | 7.22 ($\pm$0.76) | 4.25 ($\pm$0.55) |
| | 35.05 ($\pm$0.59) | 11.60 ($\pm$0.31) | 7.20 ($\pm$0.42) | 3.99 ($\pm$0.47) |
| | 37.52 ($\pm$0.76) | 13.92 ($\pm$0.69) | 6.20 ($\pm$0.61) | 6.12 ($\pm$0.59) |
| | 36.58 ($\pm$0.78) | 11.58 ($\pm$0.86) | 6.29 ($\pm$1.02) | 4.83 ($\pm$0.59) |
| | 33.84 ($\pm$0.71) | 11.69 ($\pm$0.73) | 8.33 ($\pm$0.62) | 5.72 ($\pm$0.55) |
| | 36.63 ($\pm$0.75) | 11.56 ($\pm$0.66) | 6.82 ($\pm$1.05) | 4.47 ($\pm$0.58) |
| | 37.11 ($\pm$0.73) | 12.01 ($\pm$0.40) | 6.88 ($\pm$0.54) | 4.95 ($\pm$0.54) |
| | 36.80 ($\pm$0.66) | 12.99 ($\pm$0.53) | 7.95 ($\pm$0.86) | 5.09 ($\pm$0.50) |
| average atomic composition (only metals included) / % | 36.24 ($\pm$0.72) | 12.17 ($\pm$0.61) | 7.11 ($\pm$0.73) | 4.29 ($\pm$0.55) |
| relative atomic composition (only metals included, calculated for 2 Dy centers) | 5.96 ($\pm$0.11) | 2 | 1.16 ($\pm$0.12) | 0.81 ($\pm$0.09) |
| proposed metal composition | **6** | **2** | **1.2** | **0.8** |
| compound **Dy$_2$Fe$_{0.8}$Ru$_{1.2}$** | | | | |
| measured atomic composition (only selected atom included, independent measurements) / | 38.41 ($\pm$0.74) | 13.00 ($\pm$0.69) | 4.61 ($\pm$0.76) | 7.85 ($\pm$0.55) |
| | 35.05 ($\pm$0.59) | 12.60 ($\pm$0.31) | 4.98 ($\pm$0.42) | 8.57 ($\pm$0.47) |

| % | 35.52 ($\pm$0.76) | 11.92 ($\pm$0.69) | 4.21 ($\pm$0.61) | 6.69 ($\pm$0.59) |
|---|---|---|---|---|
| | 37.58 ($\pm$0.78) | 10.58 ($\pm$0.86) | 5.74 ($\pm$1.02) | 6.82 ($\pm$0.59) |
| | 37.84 ($\pm$0.71) | 11.69 ($\pm$0.73) | 4.33 ($\pm$0.62) | 5.47 ($\pm$0.55) |
| | 36.63 ($\pm$0.75) | 10.56 ($\pm$0.66) | 6.02 ($\pm$1.05) | 8.47 ($\pm$0.58) |
| | 35.11 ($\pm$0.73) | 15.01 ($\pm$0.40) | 4.58 ($\pm$0.54) | 7.25 ($\pm$0.54) |
| | 35.80 ($\pm$0.66) | 11.99 ($\pm$0.53) | 5.65 ($\pm$0.86) | 6.09 ($\pm$0.50) |
| average atomic composition (only metals included) / % | 36.49 ($\pm$0.72) | 12.17 ($\pm$0.61) | 5.02 ($\pm$0.74) | 7.15 ($\pm$0.55) |
| relative atomic composition (only metals included, calculated for 2 Dy centers) | 6.00 ($\pm$0.12) | 2 | 0.82 ($\pm$0.12) | 1.18 ($\pm$0.09) |
| proposed metal composition | **6** | **2** | **0.8** | **1.2** |
| compound **Dy$_2$Ru$_2$** | | | | |
| measured atomic composition (only selected atom included, independent measurements) / % | 35.10 ($\pm$1.07) | 12.07 ($\pm$0.89) | – | 9.84 ($\pm$0.77) |
| | 34.60 ($\pm$0.85) | 12.71 ($\pm$0.66) | – | 11.43 ($\pm$1.21) |
| | 33.97 ($\pm$0.74) | 11.11 ($\pm$0.52) | – | 12.78 ($\pm$1.00) |
| | 35.60 ($\pm$1.01) | 10.99 ($\pm$0.95) | – | 12.66 ($\pm$0.82) |
| | 35.69 ($\pm$0.88) | 11.46 ($\pm$0.62) | – | 10.54 ($\pm$0.90) |
| | 36.51 ($\pm$0.54) | 12.67 ($\pm$0.30) | – | 11.44 ($\pm$0.69) |
| | 36.40 ($\pm$0.96) | 13.65 ($\pm$0.76) | – | 14.03 ($\pm$1.31) |
| | 36.54 ($\pm$0.73) | 11.49 ($\pm$0.59) | – | 12.10 ($\pm$1.07) |
| average atomic composition (only metals included) / % | 35.55 ($\pm$0.85) | 12.02 ($\pm$0.66) | – | 11.85 ($\pm$0.97) |
| relative atomic composition (only metals included, calculated for 2 Dy centers) | 5.92 ($\pm$0.14) | 2 | – | 1.97 ($\pm$0.16) |
| proposed metal composition | **6** | **2** | – | **2** |
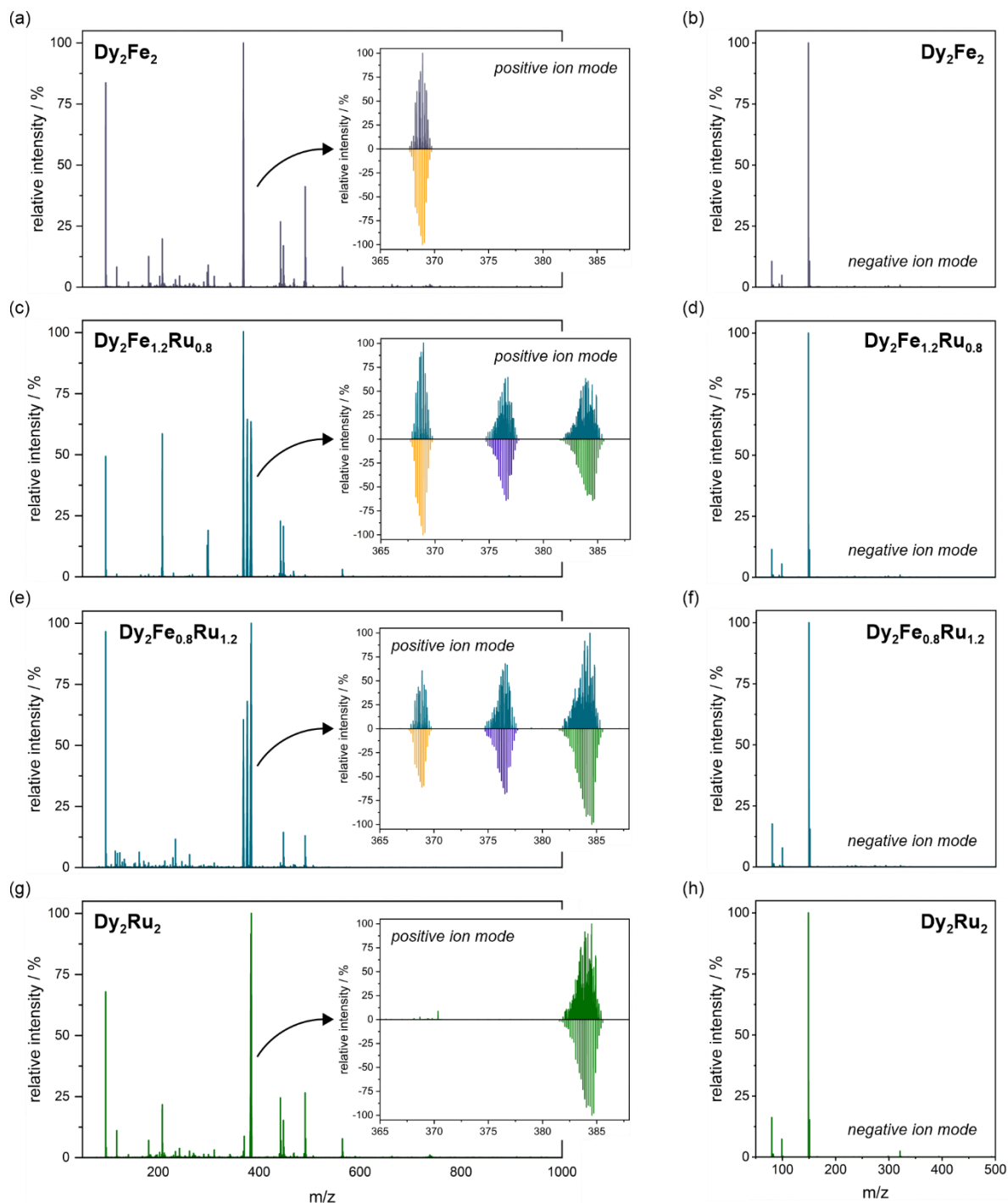
**Fig. S1** The electrospray ionization mass spectra (ESI-MS) of **Dy$_2$Fe$_2$** (a, b),[S3] **Dy$_2$Fe$_{1.2}$Ru$_{0.8}$** (c, d), **Dy$_2$Fe$_{0.8}$Ru$_{1.2}$** (e, f), and **Dy$_2$Ru$_2$** (g, h) in methanol, measured in positive (left panel) and negative (right panel) ion mode. Inside the spectra in left panel, the limited m/z range of 365–388 of the spectra is presented, and compared with calculated distributions for corresponding theoretical complexes: {[Dy(4-pyone)$_5$]$_2$[Fe(CN)$_2$(phen)$_2$]$_2$}$^{6+}$ (orange), {[Dy(4-pyone)$_5$]$_2$[Fe(CN)$_2$(phen)$_2$]$_1$[Ru(CN)$_2$(phen)$_2$]$_1$}$^{6+}$ (violet), and {[Dy(4-pyone)$_5$]$_2$[Ru(CN)$_2$(phen)$_2$]$_2$}$^{6+}$ (green).

Comment to Fig. S1: The thorough analysis of the mass spectra for **Dy$_2$Fe$_2$** is considered in detail in Ref. S3. Here, for the spectra of their structural analogs containing Ru(2+) ions, we used this technique to determine the ratio between metals in hetero-bi-metallic **Dy$_2$Ru$_2$** as well as hetero-tri-metallic **Dy$_2$Fe$_{1.2}$Ru$_{0.8}$** and **Dy$_2$Fe$_{0.8}$Ru$_{1.2}$**. The results of this analysis are in agreement with the EDS data and are presented in Table S2. Moreover, the mass-spectrometry reveals that **Dy$_2$Fe$_{2-x}$Ru$_x$** phases are built up from 3 different units, both hetero-bi-metallic units (only Dy/Fe- and Dy/Ru-containing, {Dy$_2$Fe$_2$} and {Dy$_2$Ru$_2$}, respectively), as well as hetero-tri-metallic {Dy$_2$Fe$_1$Ru$_1$} unit.

**Table S2** Results of relative atomic composition determined from mass spectra compared with those obtained from energy dispersive X-ray microanalysis for compounds $Dy_2Fe_2$,[S3] $Dy_2Fe_{1.2}Ru_{0.8}$, $Dy_2Fe_{0.8}Ru_{1.2}$, and $Dy_2Ru_2$.

| compound | metal | relative atomic composition | | | proposed metal composition |
|---|---|---|---|---|---|
| | | EDXMA (normalized for two Dy centers) | MS (normalized for two d-metal centers) | average | |
| $Dy_2Fe_2$ (as a reference compound)[S3] | Fe | 1.97 ($\pm$0.10) | 2 | 1.985 ($\pm$0.10) | **2** |
| | Ru | – | – | – | – |
| $Dy_2Fe_{1.2}Ru_{0.8}$ | Fe | 1.16 ($\pm$0.12) | 1.158 ($\pm$0.01) | 1.159 ($\pm$0.07) | **1.2** |
| | Ru | 0.81 ($\pm$0.09) | 0.842 ($\pm$0.01) | 0.826 ($\pm$0.05) | **0.8** |
| $Dy_2Fe_{0.8}Ru_{1.2}$ | Fe | 0.82 ($\pm$0.12) | 0.830 ($\pm$0.01) | 0.825 ($\pm$0.07) | **0.8** |
| | Ru | 1.18 ($\pm$0.09) | 1.170 ($\pm$0.01) | 1.175 ($\pm$0.05) | **1.2** |
| $Dy_2Ru_2$ | Fe | – | – | – | – |
| | Ru | 1.97 ($\pm$0.16) | 2 | 1.985 ($\pm$0.16) | **2** |
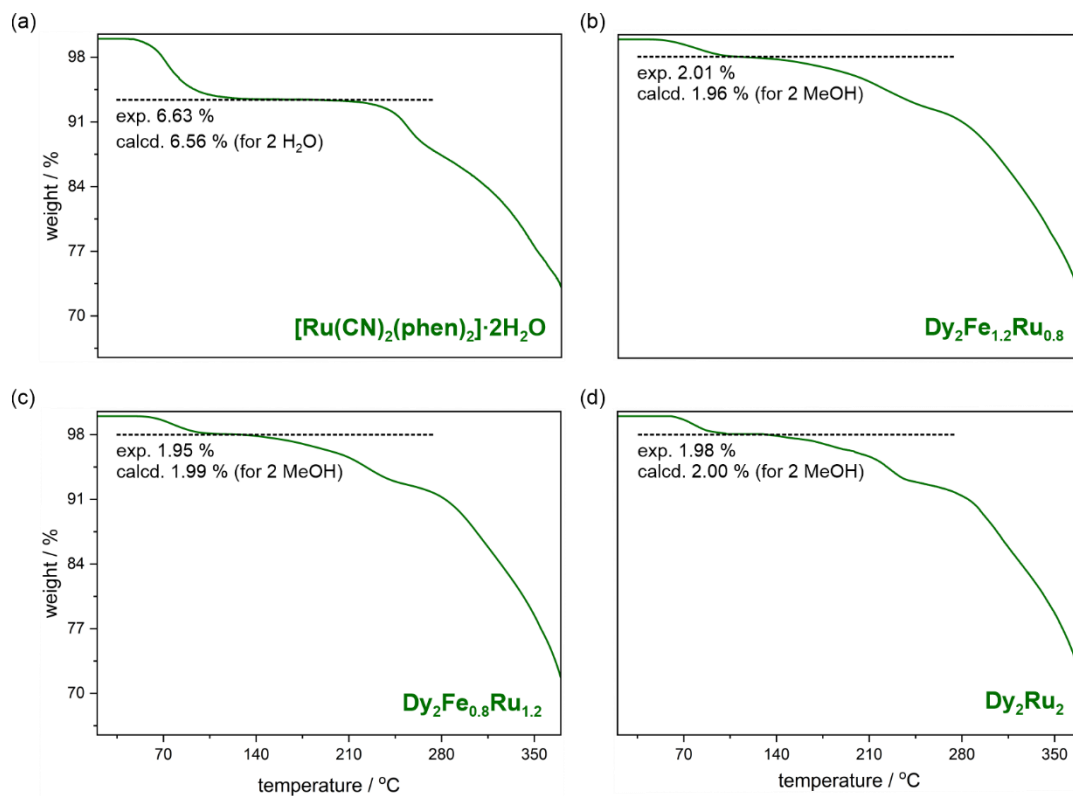
**Fig. S2** Thermogravimetric (TG) curves collected in the temperature range of 20–370 °C for crystalline samples of [Ru$^{II}$(CN)$_2$(phen)$_2$]·2H$_2$O precursor (a), **Dy$_2$Fe$_{1.2}$Ru$_{0.8}$** (b), **Dy$_2$Fe$_{0.8}$Ru$_{1.2}$** (c), and **Dy$_2$Ru$_2$** (d). The steps related to the loss of solvent molecules are depicted.
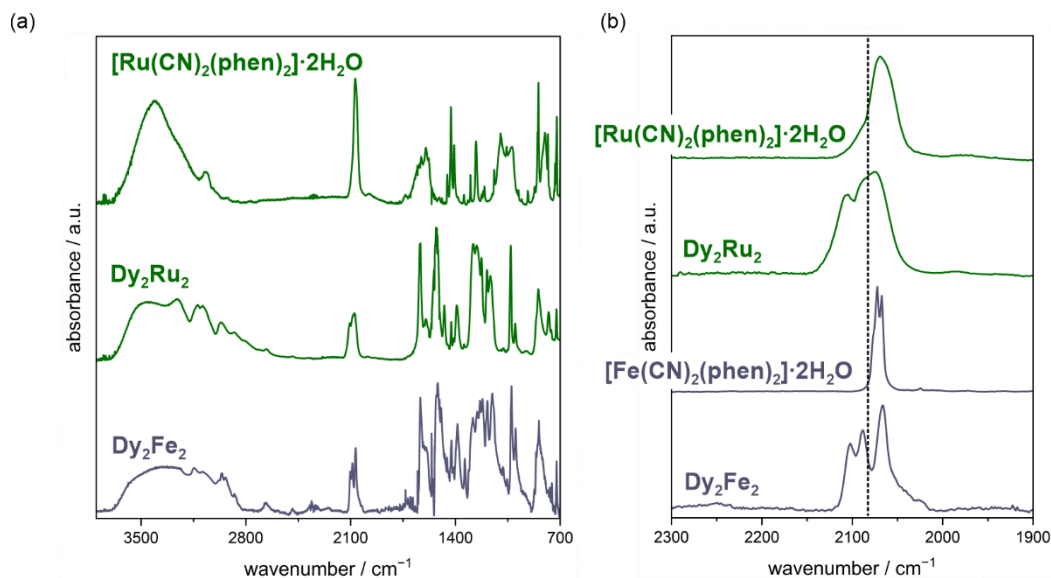
**Fig. S3** Infrared (IR) absorption spectra of the selected single crystals of [Ru$^{II}$(CN)$_2$(phen)$_2$]·2H$_2$O precursor and **Dy$_2$Ru$_2$** gathered in the 4000–700 cm$^{-1}$ range (a), together with the enlargement for the limited 2300–1900 cm$^{-1}$ region related to the characteristic stretching vibrations of cyanido ligands (b). The spectra are compared with analogous Fe(II)-based **Dy$_2$Fe$_2$** and [Fe$^{II}$(CN)$_2$(phen)$_2$]·2H$_2$O compounds (in the (a) part, only with the first one).[S3]

Comment to Fig. S3: The 1700–700 cm$^{-1}$ range, consisting of a large number of absorption peaks, is related mainly to the skeletal vibrations of phen ligands in [Ru$^{II}$(CN)$_2$(phen)$_2$]·2H$_2$O and **Dy$_2$Ru$_2$** as well as 4-pyone ligands in the hetero-bi-metallic system. The broad absorption above 2800 cm$^{-1}$ is due to the stretching $v$(C–H) and/or $v$(N–H) vibrations of organic moieties and $v$(O–H) vibrations of solvent (MeOH, H$_2$O) molecules. In the 2150–2000 cm$^{-1}$ range, the characteristic peaks related to the stretching vibrations of cyanido ligands are observed. In *cis*-[Ru$^{II}$(CN)$_2$(phen)$_2$]·2H$_2$O precursor, the absorption peaks in the range 2080–2050 cm$^{-1}$ are observed and can be assigned to terminal cyanido ligands. The band maximum position at 2069 cm$^{-1}$ is comparable to the stretching vibrations of cyanido ligands in *cis*-[Fe$^{II}$(CN)$_2$(phen)$_2$]·2H$_2$O precursor. In **Dy$_2$Ru$_2$**, all of the absorption peaks of cyanido stretching vibrations are shifted towards higher energies. Taking into account the structural data, the series of absorption peaks, in the range 2150–2080 cm$^{-1}$ can be assigned to bridging cyanido ligands, and a set of lower energy peaks below 2080 cm$^{-1}$ ascribable to terminal cyanido ligands. This interpretation stays in good agreement with the structural data and literature analysis.[S2–S4,S11]

**Table S3** Crystal data and structure refinement parameters for **Dy$_2$Fe$_{1.2}$Ru$_{0.8}$** and **Dy$_2$Fe$_{0.8}$Ru$_{1.2}$**.

| compound | Dy$_2$Fe$_{1.2}$Ru$_{0.8}$ | Dy$_2$Fe$_{0.8}$Ru$_{1.2}$ |
|---|---|---|
| formula | C$_{110}$H$_{90}$Dy$_2$F$_{18}$Fe$_{1.2}$Ru$_{0.8}$N$_{22}$O$_{30}$S$_6$ | C$_{110}$H$_{90}$Dy$_2$F$_{18}$Fe$_{0.8}$Ru$_{1.2}$N$_{22}$O$_{30}$S$_6$ |
| form. weight / g·mol$^{-1}$ | 3207.27 | 3217.3 |
| $\lambda$ / Å | 0.71073 Å (Mo K$\alpha$) | |
| $T$ / K | 100(2) | |
| crystal system | triclinic | |
| space group | $P-1$ (No. 2) | |
| $a$ / Å | 12.7322(12) | 12.4917(17) |
| $b$ / Å | 14.8109(13) | 14.753(2) |
| $c$ / Å | 18.7471(16) | 19.084(3) |
| $\alpha$ / deg. | 66.821(3) | 69.179(4) |
| $\beta$ / deg. | 83.203(3) | 83.711(4) |
| $\gamma$ / deg. | 71.337(3) | 71.745(4) |
| $V$ / Å$^3$ | 3078.9(5) | 3121.8(7) |
| $Z$ | 1 | 1 |
| calcd. density / g·cm$^{-1}$ | 1.730 | 1.711 |
| abs. coeff. / cm$^{-1}$ | 1.648 | 1.627 |
| $F$(000) | 1600 | 1600 |
| $\Theta$ range / deg. | 2.565–25.028 | 2.503–25.027 |
| collected refl. | 34187 | 35906 |
| limiting indices | $-15 < h < 15$<br>$-17 < k < 17$<br>$-22 < l < 22$ | $-14 < h < 14$<br>$-17 < k < 17$<br>$-22 < l < 22$ |
| $R_{int}$ | 0.0381 | 0.0648 |
| completeness / % | 99.8 | 99.8 |
| data/restraints/param. | 10853/37/856 | 11023/288/1099 |
| GOF on $F^2$ | 1.064 | 1.096 |
| final $R_1$ [$I > 2\sigma(I)$] | 0.0454 | 0.0739 |
| final w$R_2$ [all data] | 0.1143 | 0.1751 |
| diff. peak and hole / e·Å$^{-3}$ | 1.650 and $-2.319$ | 2.494 and $-3.326$ |
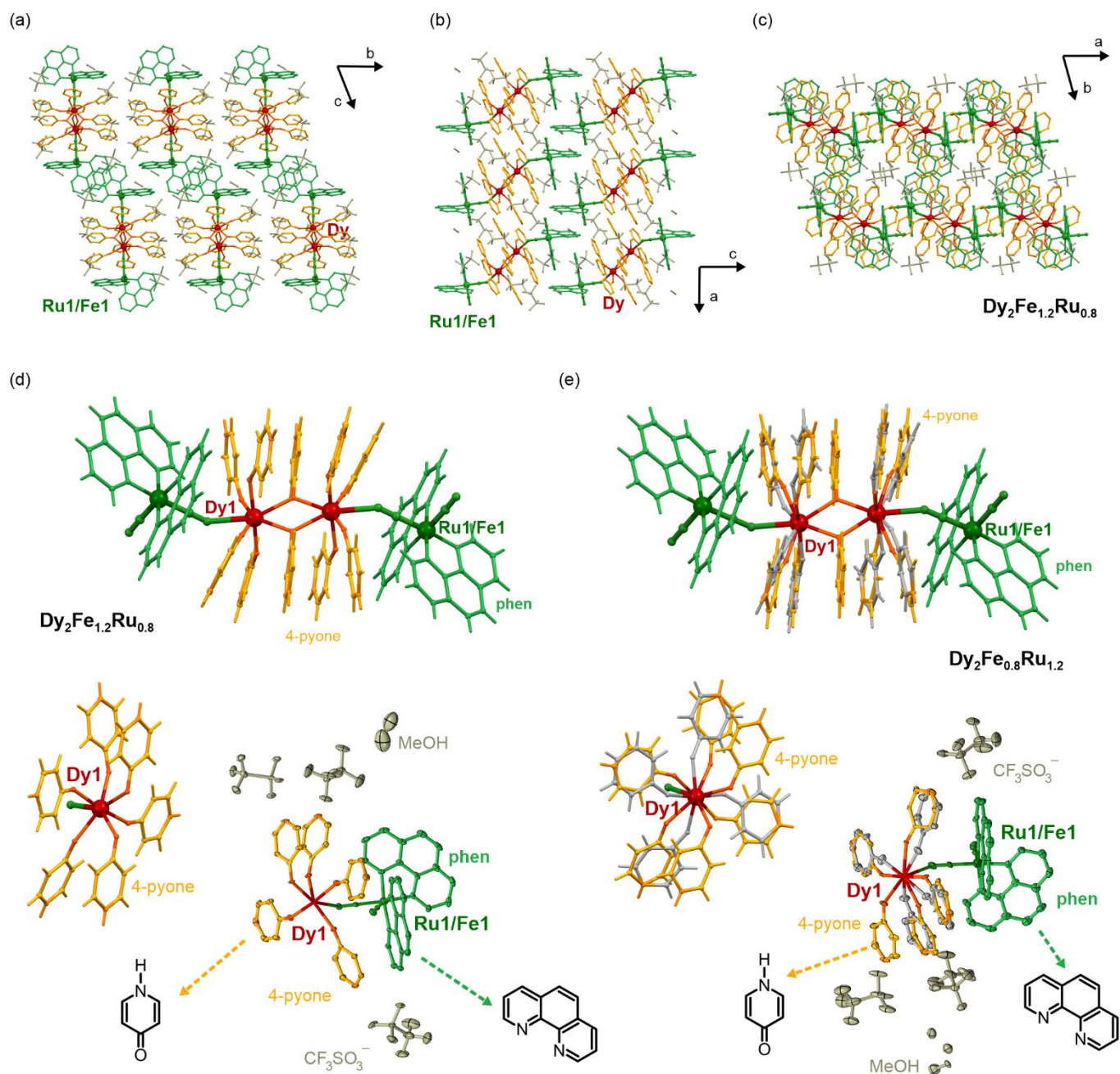
**Fig. S4** Detailed structural views of **Dy$_2$Fe$_{1.2}$Ru$_{0.8}$** and **Dy$_2$Fe$_{0.8}$Ru$_{1.2}$**: the representative views of the supramolecular network along the crystallographic *a* axis (a), *b* axis (b), and *c* axis (c) on the example of the crystal structure of **Dy$_2$Fe$_{1.2}$Ru$_{0.8}$** (analogous views are observed for **Dy$_2$Fe$_{0.8}$Ru$_{1.2}$**) and the enlarged view of tetrametallic {Dy$^{III}_2$Fe$^{II}_{1.2}$Ru$^{II}_{0.8}$}$^{6+}$ and {Dy$^{III}_2$Fe$^{II}_{0.8}$Ru$^{II}_{1.2}$}$^{6+}$ molecular cation, shown together with the coordination sphere of seven-coordinated Dy$^{III}$ complexes, as well as the asymmetric unit for **Dy$_2$Fe$_{1.2}$Ru$_{0.8}$** (d) and **Dy$_2$Fe$_{0.8}$Ru$_{1.2}$** (e). The hydrogen atoms in some views are omitted for clarity. Thermal ellipsoids in (e) (in the asymmetric units) are presented at the 50% probability level. Detailed structure parameters are gathered in Table S4. In the crystal structure with a predominance of Ru(II) centers, i.e., **Dy$_2$Fe$_{0.8}$Ru$_{1.2}$**, a few equivalent positions of 4-pyone ligands as well as solvent molecules and anions were marked in different colors. The structural diagrams for the used organic ligands were added in the asymmetric units in (d) and (e).

**Table S4** Detailed structure parameters of $Dy^{III}$ and $Fe^{II}/Ru^{II}$ complexes in $Dy_2Fe_2$,[S3] $Dy_2Fe_{1.2}Ru_{0.8}$, and $Dy_2Fe_{0.8}Ru_{1.2}$.

| distance or angle | $Dy_2Fe_2$[S3] | $Dy_2Fe_{1.2}Ru_{0.8}$ | $Dy_2Fe_{0.8}Ru_{1.2}$ |
|---|---|---|---|
| distances and angles in dysprosium(III) complexes / Å,° | | | |
| Dy1–O1 | 2.4008(14)/ 2.4207(15) | 2.409(3)/2.425(3) | 2.407(6)/2.411(6) |
| Dy1–O2 | 2.2897(15) | 2.296(3) | 2.272(13)/2.289(11) |
| Dy1–O3 | 2.2286(15) | 2.249(4) | 2.227(11)/2.253(14) |
| Dy1–O4 | 2.2767(15) | 2.284(3) | 2.287(14)/2.294(11) |
| Dy1–O5 | 2.2312(15) | 2.251(4) | 2.215(13)/2.246(11) |
| Dy1–N1 | 2.4910(18) | 2.499(4) | 2.507(8) |
| O1–Dy1–O1 | 63.37(6) | 63.33(13) | 63.4(2) |
| O1–Dy1–O2 | 81.06(5)/141.46(5) | 80.89(12)/141.37(12) | 82.0(4)/75.5(3) |
| O1–Dy1–O3 | 79.60(6)/ 98.40(6) | 79.72(13)/98.03(13) | 82.3(3)/137.2(3)/ 92.8(3)/75.8(4) |
| O1–Dy1–O4 | 130.63(5)/72.29(5) | 130.65(12)/72.29(12) | 79.3(3)/125.7(4)/ 142.0(3) |
| O1–Dy1–O5 | 99.87(6)/87.67(5) | 99.43(13)/88.12(12) | 99.1(4)/104.0(4)/ 90.1(3) |
| O1–Dy1–N1 | 152.47(5)/143.59(5) | 152.50(13)/143.56(13) | 146.4(2)/149.3(2) |
| O2–Dy1–O3 | 88.69(6) | 88.90(13) | 88.4(5)/88.2(4) |
| O2–Dy1–O4 | 146.20(5) | 146.31(13) | 148.9(5)/142.4(4) |
| O2–Dy1–O5 | 84.14(6) | 83.63(13) | 83.9(6)/92.4(4) |
| O2–Dy1–N1 | 73.97(6) | 74.17(14) | 73.3(4)/73.7(3) |
| O3–Dy1–O4 | 86.71(6) | 86.39(13) | 86.0(5)/ 88.7(4) |
| O3–Dy1–O5 | 172.80(5) | 172.51(13) | 177.1(4)/172.2(5) |
| O3–Dy1–N1 | 88.31(6) | 88.31(14) | 86.9(4)/85.4(4) |
| O4–Dy1–O5 | 98.89(6) | 99.60(13) | 100.1(6)/89.1(4) |
| O4–Dy1–N1 | 72.44(6) | 72.36(13) | 75.8(4)/68.7(3) |
| O5–Dy1–N1 | 89.07(6) | 89.24(14) | 91.4(4)/90.5(4) |
| distances and angles in iron(II)/ruthenium(II) complexes / Å,° | | | |
| Fe1/Ru1–C1 | 1.890(2) | 1.902(5) | 1.893(10) |
| Fe1/Ru1–C2 | 1.893(2) | 1.910(5) | 1.901(10) |
| Fe1/Ru1–N3 | 1.9694(19) | 1.973(4) | 1.982(8) |
| Fe1/Ru1–N4 | 2.0052(19) | 2.008(4) | 2.011(7) |

| | | | |
|---|---|---|---|
| Fe1/Ru1–N5 | 2.0030(19) | 2.007(4) | 2.007(8) |
| Fe1/Ru1–N6 | 1.9751(19) | 1.977(4) | 1.989(8) |
| C1– Fe1/Ru1–C2 | 88.78(9) | 88.5(2) | 88.6(4) |
| C1– Fe1/Ru1–N3 | 94.23(9) | 94.3(2) | 94.3(4) |
| C1– Fe1/Ru1–N4 | 175.75(8) | 175.8(2) | 175.6(4) |
| C1– Fe1/Ru1–N5 | 91.37(8) | 91.5(2) | 91.4(4) |
| C1– Fe1/Ru1–N6 | 91.57(8) | 91.6(2) | 92.3(3) |
| C2– Fe1/Ru1–N3 | 91.31(8) | 91.3(2) | 90.3(3) |
| C2– Fe1/Ru1–N4 | 93.00(8) | 93.33(19) | 93.4(4) |
| C2– Fe1/Ru1–N5 | 175.02(9) | 175.3(2) | 175.6(4) |
| C2– Fe1/Ru1–N6 | 92.70(9) | 92.8(2) | 93.4(3) |
| N3– Fe1/Ru1–N4 | 81.88(8) | 81.95(18) | 81.8(3) |
| N3– Fe1/Ru1–N5 | 93.64(8) | 93.41(18) | 93.7(3) |
| N3– Fe1/Ru1–N6 | 173.02(8) | 172.98(18) | 173.2(3) |
| N4– Fe1/Ru1–N5 | 87.19(7) | 86.98(17) | 85.4(3) |
| N4– Fe1/Ru1–N6 | 92.20(8) | 92.10(18) | 92.9(4) |
| N5– Fe1/Ru1–N6 | 82.32(8) | 82.50(18) | 82.3(3) |
| distances and angles between dysprosium(III) and iron(II)/ruthenium(II) centers within $\{Dy_2(Fe/Ru)_2\}^{6+}$ molecular cations / Å, º | | | |
| Dy1···Dy1 | 4.103(4) | 4.114(9) | 4.099(16) |
| Dy1–O1–Dy1 | 116.63(6) | 116.66(6) | 116.59(6) |
| Dy1···Fe1/Ru1 | 5.263(4) | 5.265(9) | 5.287(16) |
| Dy1–N1–C1 | 142.87(6) | 142.48(6) | 144.28(6) |
| distances and angles between dysprosium(III) and iron(II)/ruthenium(II) centers between $\{Dy_2(Fe/Ru)_2\}^{6+}$ molecular cations (the shortest distance)/ Å, º | | | |
| Dy1···Dy1 | 9.983(5) | 9.982(5) | 9.870(5) |
| Fe1/Ru1···Fe1/Ru1 | 8.857(5) | 8.847(5) | 8.998(5) |

**Table S5** Results of Continuous Shape Measure (CShM) analysis for six-coordinated iron(II)/ruthenium(II) and seven-coordinated dysprosium(III) complexes in the crystal structures of **$Dy_2Fe_2$,**[S3] **$Dy_2Fe_{1.2}Ru_{0.8}$,** and **$Dy_2Fe_{0.8}Ru_{1.2}$.**[S13,S14]

| compound | CShM parameters* for six-coordinated Fe(II)/Ru(II) complexes, $[Fe^{II}/Ru^{II}(\mu-CN)(CN)(phen)_2]$ | | | |
|---|---|---|---|---|
| | HP-6 | PPY-6 | OC-6 | TPR-6 |
| **$Dy_2Fe_2$**[S3] | 30.086 | 27.747 | **0.308** | 14.957 |
| **$Dy_2Fe_{1.2}Ru_{0.8}$** | 30.032 | 27.739 | **0.314** | 14.959 |
| **$Dy_2Fe_{0.8}Ru_{1.2}$** | 29.501 | 27.430 | **0.320** | 15.075 |

| compound | CShM parameters* for seven-coordinated Dy(III) complexes, $[Dy^{III}(\mu-NC)(4\text{-pyone})_6]^{2+}$ | | | | |
|---|---|---|---|---|---|
| | HP-7 | HPY-7 | PBPY-7 | COC-7 | CTPR-7 |
| **$Dy_2Fe_2$**[S3] | 32.717 | 23.395 | **1.344** | 4.403 | 3.692 |
| **$Dy_2Fe_{1.2}Ru_{0.8}$** | 32.983 | 23.499 | **1.421** | 4.416 | 3.765 |
| **$Dy_2Fe_{0.8}Ru_{1.2}$** | 32.369 | 23.631 | **1.552** | 4.890 | 3.623 |

*CShM parameters for six- and seven-coordinated metal complexes: [S13,S14]

**for six-coordinated complexes:**

| | | |
|---|---|---|
| CShM HP-6 | – | the parameter related to the hexagon geometry ($D_{6h}$ symmetry) |
| CShM PPY-6 | – | the parameter related to the pentagonal pyramid geometry ($C_{5v}$ symmetry) |
| CShM OC-6 | – | the parameter related to the octahedron geometry ($O_h$ symmetry) |
| CShM TPR-6 | – | the parameter related to the trigonal prism geometry ($D_{3h}$ symmetry) |

**for seven-coordinated complexes:**

| | | |
|---|---|---|
| CShM HP-7 | – | the parameter related to the heptagon geometry ($D_{7h}$ symmetry) |
| CShM HPY-7 | – | the parameter related to the hexagonal pyramid geometry ($C_{6v}$ symmetry) |
| CShM PBPY-7 | – | the parameter related to the pentagonal bipyramid $D_{5h}$ geometry ($D_{5h}$ symmetry) |
| CShM COC-7 | – | the parameter related to the capped octahedron geometry ($C_{3v}$ symmetry) |
| CShM CTPR-7 | – | the parameter related to the capped trigonal prism geometry ($C_{2v}$ symmetry) |

The value of CShM = 0 is ascribed to the ideal geometry. The increase of the CShM parameter above 0 represents the increasing distortion from the ideal polyhedron.
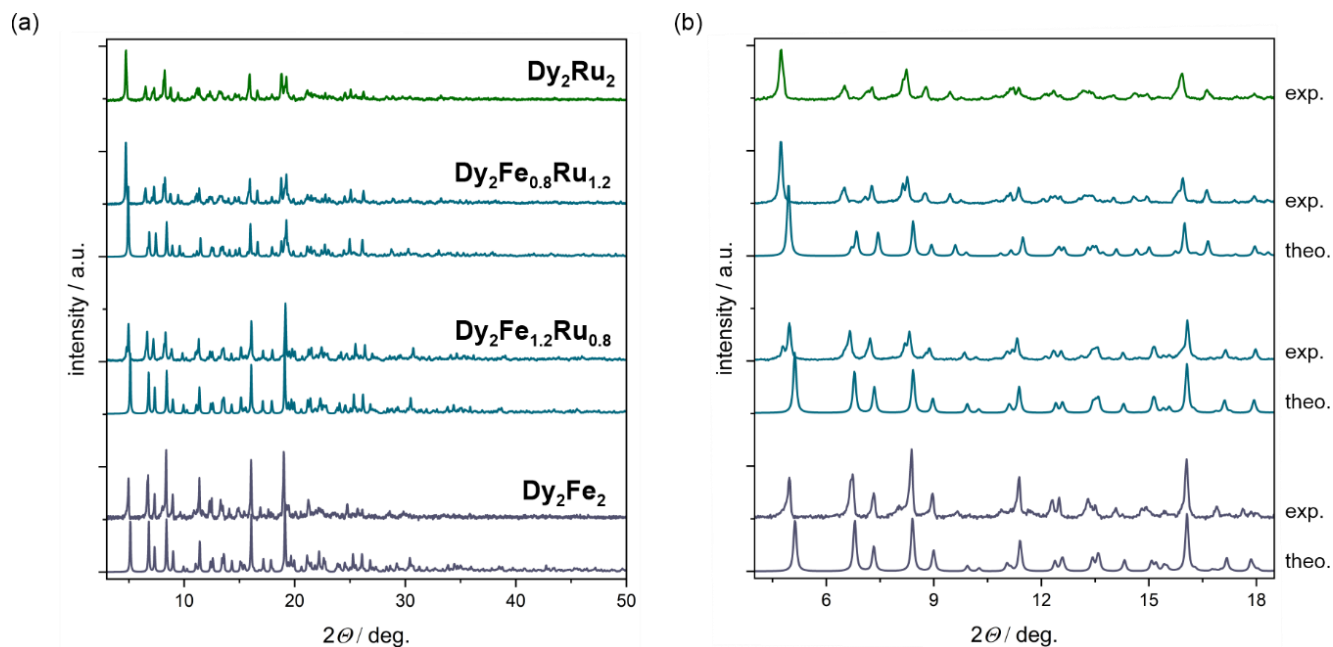
**Fig. S5** Experimental room-temperature powder X-ray diffraction (P-XRD) patterns of **Dy₂Fe₂**,[S3] **Dy₂Fe₁.₂Ru₀.₈, Dy₂Fe₀.₈Ru₁.₂,** and **Dy₂Ru₂,** presented in the broad $2\Theta$ range of 3–50° (a) and the limited low angle region of 4–20° (b). Experimental data were compared with the patterns calculated for the respective structural models of **Dy₂Fe₂**,[S3] **Dy₂Fe₁.₂Ru₀.₈,** and **Dy₂Fe₀.₈Ru₁.₂** obtained from the SC-XRD structural analysis ($T$ = 100 K).

**Table S6** Unit cell parameters of **Dy₂Ru₂** obtained from the indexing of experimental P-XRD pattern (shown in Fig. S5), compared with the cell determination results obtained within the SC-XRD analyses of **Dy₂Fe₂,**[S3] **Dy₂Fe₁.₂Ru₀.₈,** and **Dy₂Fe₀.₈Ru₁.₂** (Table S3).

| compound | Dy$_2$Fe$_2$[S3] | Dy$_2$Fe$_{1.2}$Ru$_{0.8}$ | Dy$_2$Fe$_{0.8}$Ru$_{1.2}$ | Dy$_2$Ru$_2$ |
|---|---|---|---|---|
| determination method | SC-XRD | SC-XRD | SC-XRD | P-XRD |
| crystal system | triclinic | | | |
| space group | $P-1$ (No. 2) | | | |
| $a$ / Å | 12.73 | 12.73 | 12.49 | 12.36 |
| $b$ / Å | 14.82 | 14.81 | 14.75 | 14.62 |
| $c$ / Å | 18.74 | 18.75 | 19.08 | 19.51 |
| $\alpha$ / deg. | 66.8 | 66.8 | 69.2 | 69.5 |
| $\beta$ / deg. | 83.3 | 83.2 | 83.7 | 84.0 |
| $\gamma$ / deg. | 71.3 | 71.3 | 71.7 | 72.6 |
| $V$ / Å$^3$ | 3077.9 | 3078.9 | 3121.8 | 3151.8 |
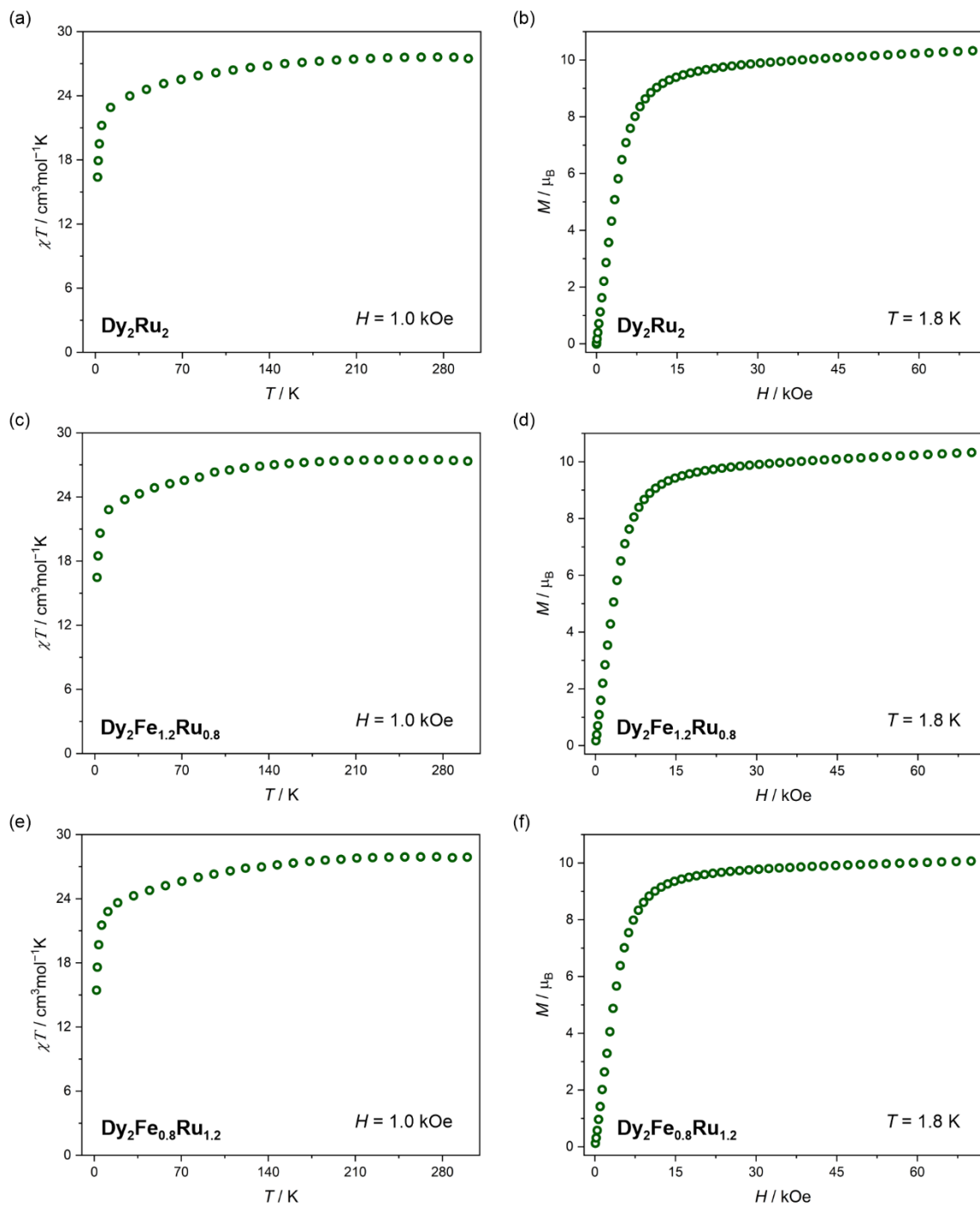
**Fig. S6** Direct-current (*dc*) magnetic characteristics for **Dy$_2$Ru$_2$** (a, b), **Dy$_2$Fe$_{1.2}$Ru$_{0.8}$** (c, d), and **Dy$_2$Fe$_{0.8}$Ru$_{1.2}$** (e, f), including the temperature dependences of the $\chi_M T$ product under the external magnetic field of $H_{dc}$ = 1000 Oe (a, c, e) and the field dependences of molar magnetization (*M*) collected at *T* = 1.8 K (b, d, f).
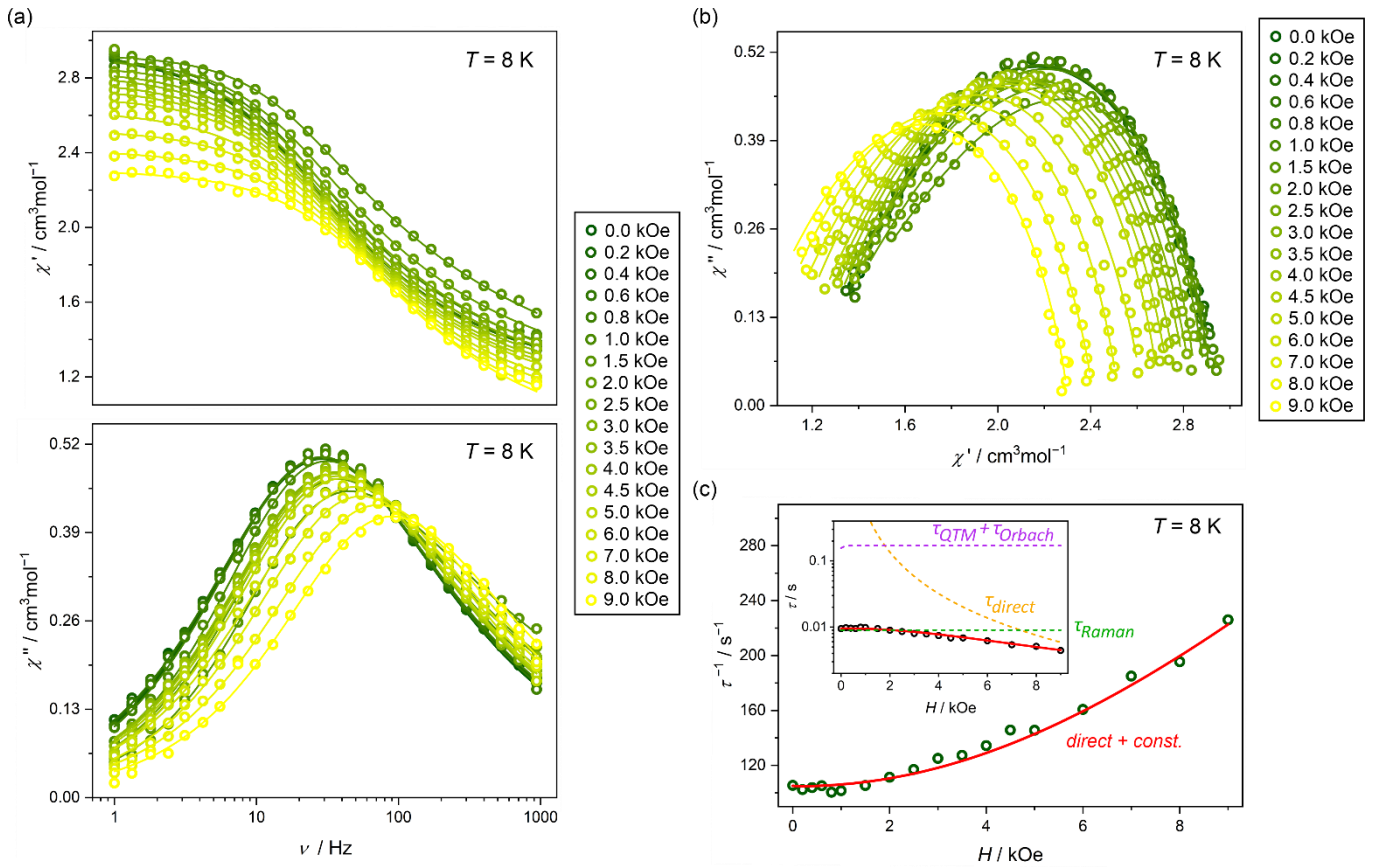
**Fig. S7** Magnetic-field-variable alternate-current (*ac*) magnetic characteristics of **Dy$_2$Ru$_2$** at 8 K, shown with the related analyses: the frequency dependences of the in-phase magnetic susceptibility, $\chi_M'$, and the out-of-phase magnetic susceptibility, $\chi_M''$, under variable indicated *dc* fields in the range of 0–10 kOe (a), the related Argand plots (b), and the *H*-dependence of resulting relaxation times, $\tau$ (c). Colored solid curves in the a–b parts represent the best fits using the generalized Debye model for a single relaxation process. The red solid line in the c part shows the best fit taking into account indicated relaxation processes (the simultaneous fit with the *T*-dependent relaxation times shown in Fig. S8), while the dashed colored lines represent the respective course of individual processes. For details see the comment below. Best-fit parameters for the c part are gathered in Table S7.
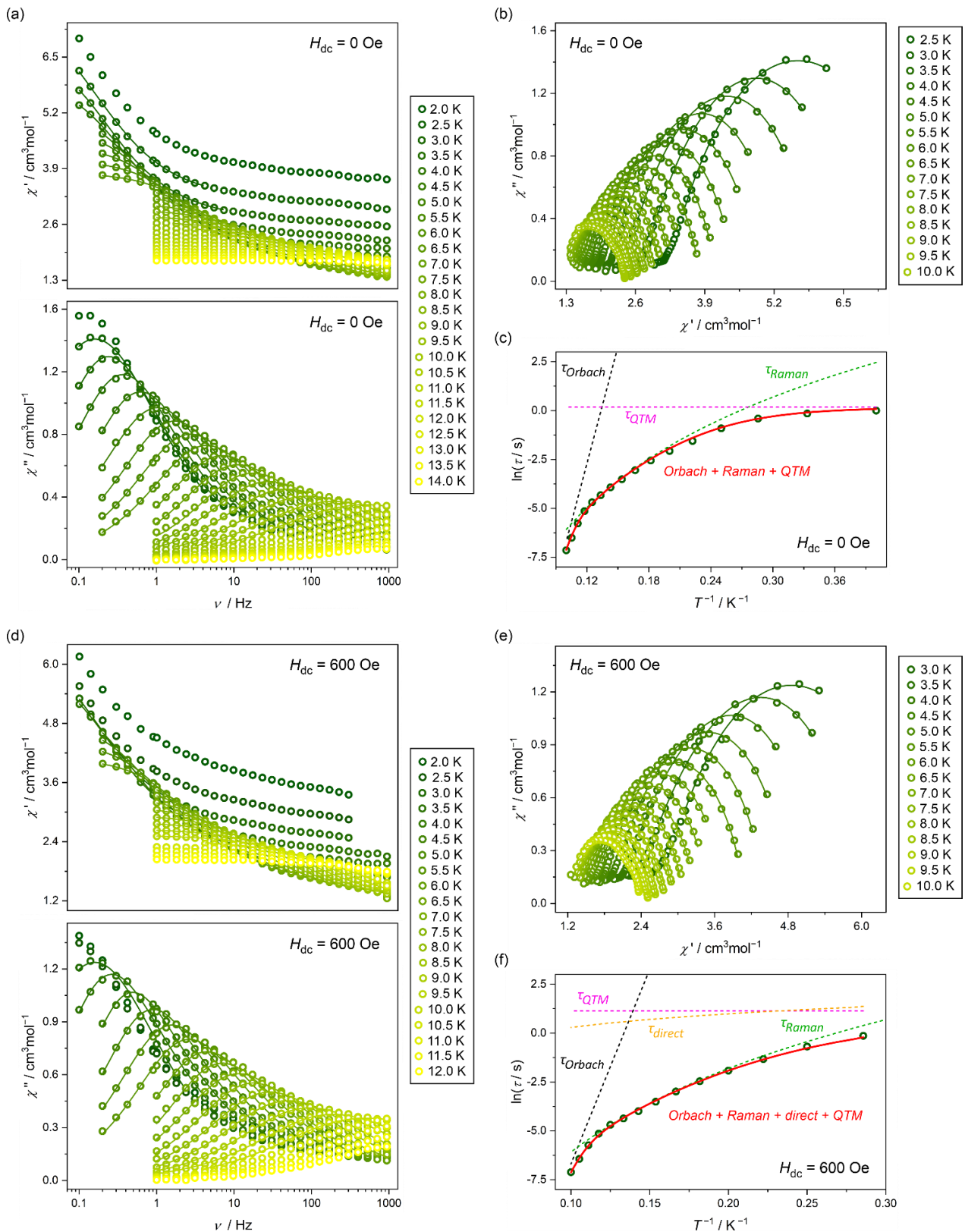
**Fig. S8** Temperature-variable alternate-current (*ac*) magnetic characteristics of **Dy₂Ru₂** under the zero and the optimal *dc* field, $H_{dc}$ of 600 Oe, shown with the related analyses: the frequency dependences of the in-phase magnetic susceptibility, $\chi_M'$, and the out-of-phase magnetic susceptibility, $\chi_M''$, under variable *T* in the range (a, d), the related Argand plots (b, e), and the temperature-dependence of resulting relaxation times (c, f). Colored solid curves in the a–b and d–e parts represent the best fits using the generalized Debye model for a single relaxation process. The red solid line in the c and f parts shows the best fit taking into account indicated relaxation processes (the simultaneous fit of both *T*-dependent relaxation times and *H*-dependent relaxation times shown in Fig. S7), while dashed colored lines represent the respective course of individual processes. Best-fit parameters for the c and f parts are gathered in Table S7.
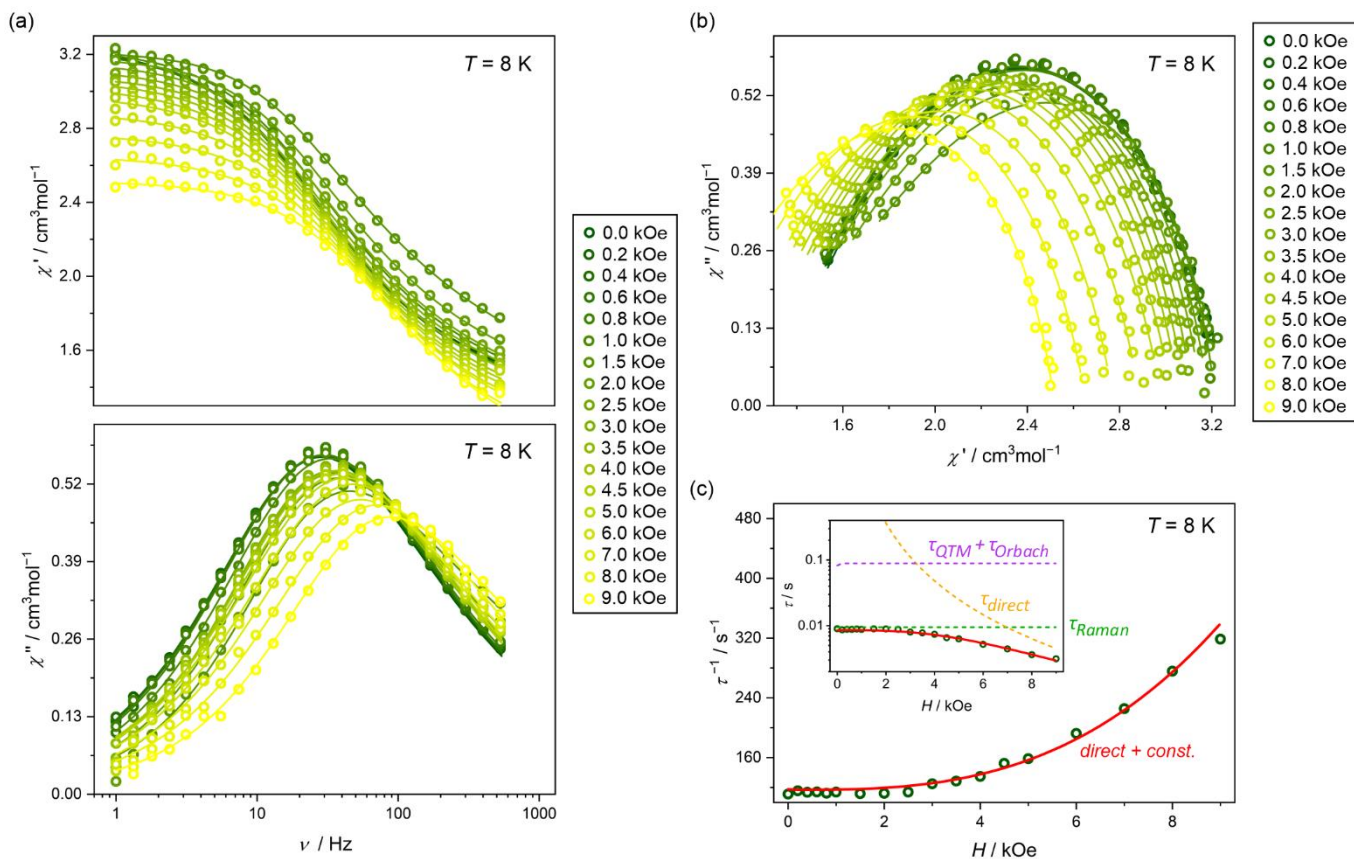
**Fig. S9** Magnetic-field-variable alternate-current (*ac*) magnetic characteristics of **Dy$_2$Fe$_{0.8}$Ru$_{1.2}$** at 8 K, shown with the related analyses: the frequency dependences of the in-phase magnetic susceptibility, $\chi_M'$, and the out-of-phase magnetic susceptibility, $\chi_M''$, under variable indicated *dc* fields in the range of 0−10 kOe (a), the related Argand plots (b), and the *H*-dependence of resulting relaxation times, $\tau$ (c). Colored solid curves in the a–b parts represent the best fits using the generalized Debye model for a single relaxation process. The red solid line in the c part shows the best fit taking into account indicated relaxation processes (the simultaneous fit with the *T*-dependent relaxation times shown in Fig. S10), while the dashed colored lines represent the respective course of individual processes. For details see the comment below. Best-fit parameters for the c part are gathered in Table S7 (see below).
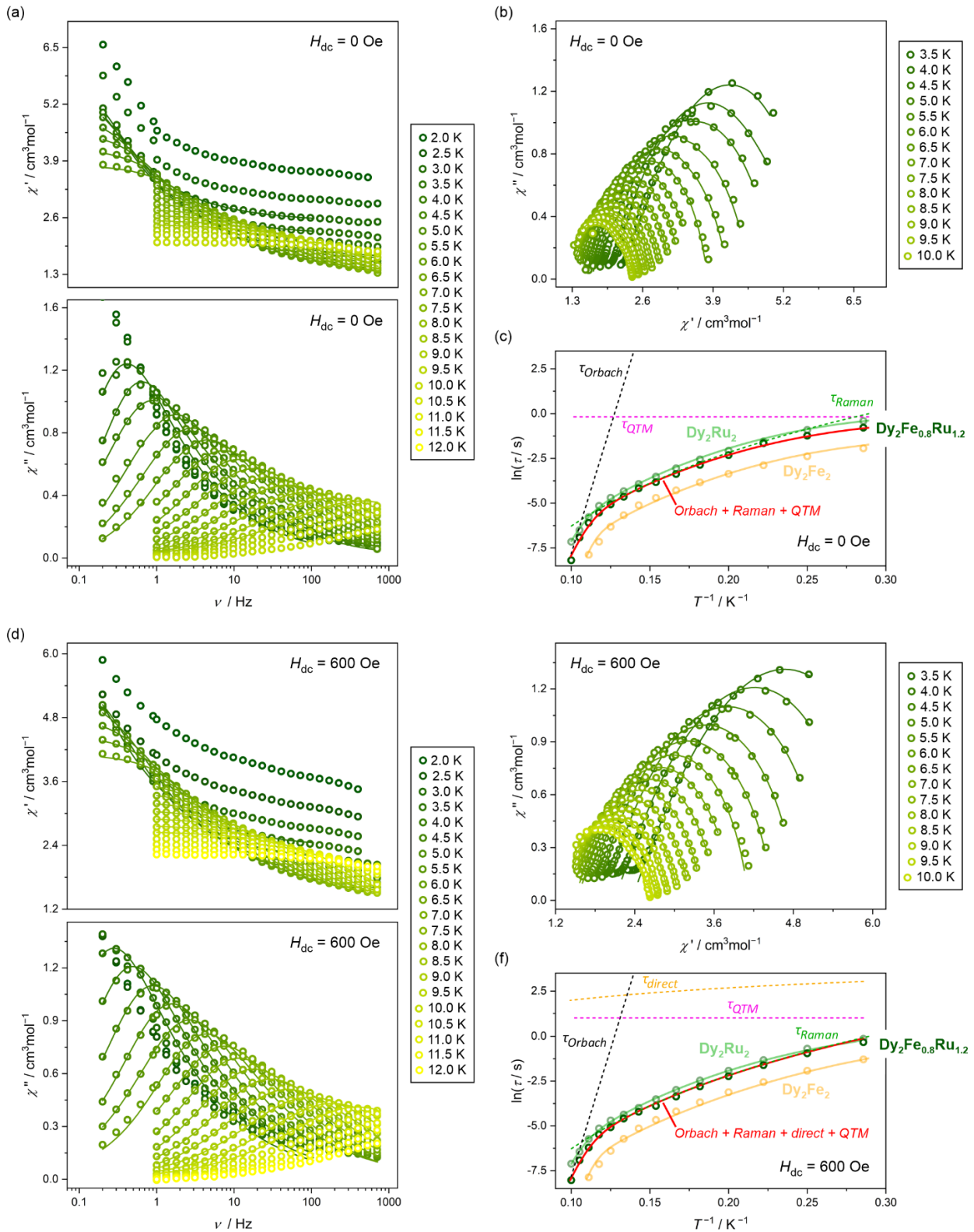
**Fig. S10** Temperature-variable alternate-current (*ac*) magnetic characteristics of **Dy₂Fe₀.₈Ru₁.₂** under the zero and the optimal *dc* field, $H_{dc}$ of 600 Oe, shown with the related analyses: the frequency dependences of the in-phase magnetic susceptibility, $\chi_M'$, and the out-of-phase magnetic susceptibility, $\chi_M''$, under variable *T* in the range (a, d), the related Argand plots (b, e), and the temperature-dependence of resulting relaxation times (c, f), compared with the *T*-dependences of relaxation time determined for the **Dy₂Ru₂** and **Dy₂Fe₂** analogs. Colored solid curves in the a–b and d–e parts represent the best fits using the generalized Debye model for a single relaxation process. The red solid line in the c and f parts shows the best fit taking into account indicated relaxation processes (the simultaneous fit of both *T*-dependent relaxation times and *H*-dependent relaxation times shown in Fig. S9), while dashed colored lines represent the respective course of individual processes. Best-fit parameters for the c and f parts are gathered in Table S7 (see below).
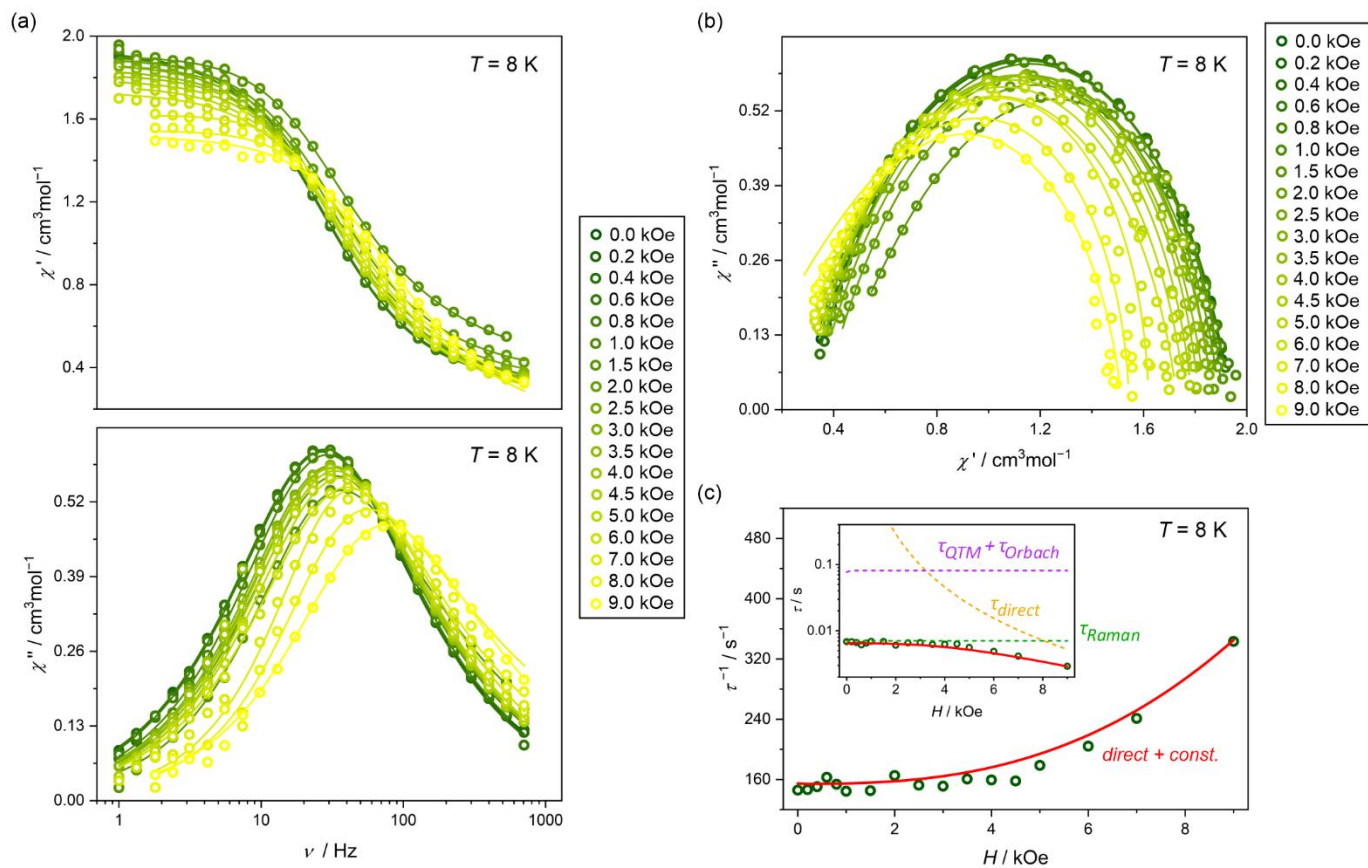
**Fig. S11** Magnetic-field-variable alternate-current (*ac*) magnetic characteristics of **Dy$_2$Fe$_{1.2}$Ru$_{0.8}$** at 8 K, shown with the related analyses: the frequency dependences of the in-phase magnetic susceptibility, $\chi_M'$, and the out-of-phase magnetic susceptibility, $\chi_M''$, under variable indicated *dc* fields in the range of 0–10 kOe (a), the related Argand plots (b), and the *H*-dependence of resulting relaxation times, $\tau$ (c). Colored solid curves in the a–b parts represent the best fits using the generalized Debye model for a single relaxation process. The red solid line in the c part shows the best fit taking into account indicated relaxation processes (the simultaneous fit with the *T*-dependent relaxation times shown in Fig. S12), while the dashed colored lines represent the respective course of individual processes. For details see the comment below. Best-fit parameters for the c part are gathered in Table S7 (see below).
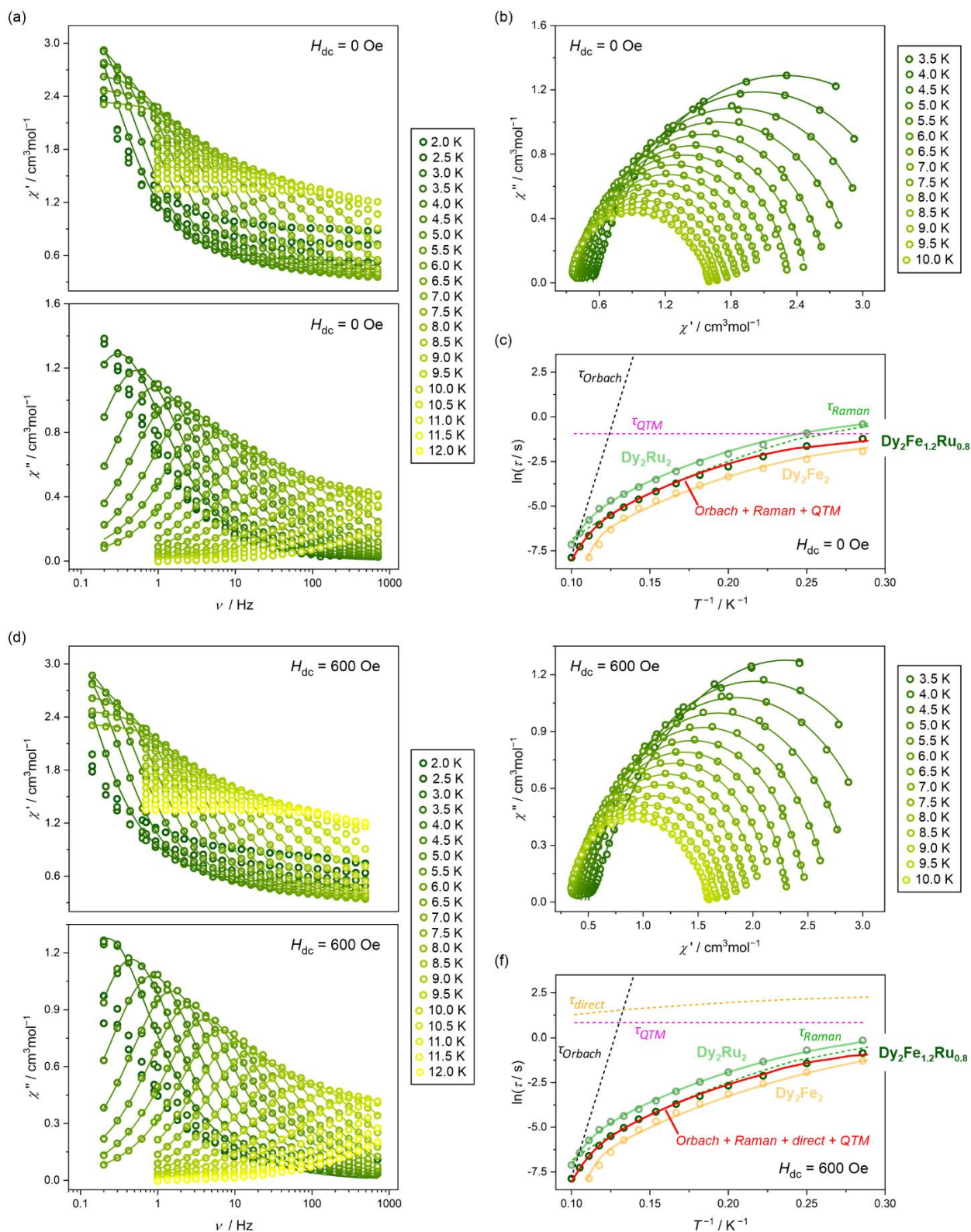
**Fig. S12** Temperature-variable alternate-current (*ac*) magnetic characteristics of **Dy₂Fe₁.₂Ru₀.₈** under the zero and the optimal *dc* field, $H_{dc}$ of 600 Oe, shown with the related analyses: the frequency dependences of the in-phase magnetic susceptibility, $\chi_M'$, and the out-of-phase magnetic susceptibility, $\chi_M''$, under variable *T* in the range (a, d), the related Argand plots (b, e), and the temperature-dependence of resulting relaxation times (c, f), compared with the *T*-dependences of relaxation time determined for the **Dy₂Ru₂** and **Dy₂Fe₂** analogs. Colored solid curves in the a–b and d–e parts represent the best fits using the generalized Debye model for a single relaxation process. The red solid line in the c and f parts shows the best fit taking into account indicated relaxation processes (the simultaneous fit of both *T*-dependent relaxation times and *H*-dependent relaxation times shown in Fig. S11), while dashed colored lines represent the respective course of individual processes. Best-fit parameters for the c and f parts are gathered in Table S7 (see below).

**Table S7** Summary of the critical slow magnetic relaxation parameters for **Dy₂Ru₂**, **Dy₂Fe₀.₈Ru₁.₂**, and **Dy₂Fe₁.₂Ru₀.₈** obtained within the three-dimensional simultaneous fitting of the field- and temperature-dependences of relaxation time (see Fig. S7–S12), compared with the results published for the **Dy₂Fe₂** analog.[S3] The details of applied fitting procedures are discussed below.

| parameter | Dy₂Fe₂[S3] | Dy₂Fe₁.₂Ru₀.₈ | Dy₂Fe₀.₈Ru₁.₂ | Dy₂Ru₂ | |
|---|---|---|---|---|---|
| | fitting with fixed $\Delta E$ (*ab initio calc.*) | | | | fitting with free $\Delta E$ |
| $A_{direct}$ / s$^{-1}$ K$^{-1}$ Oe$^{-m}$ | 1.00(3)·10$^{-10}$ | 7.46(1)·10$^{-10}$ | 1.43(5)·10$^{-9}$ | 1.20(3)·10$^{-7}$ | 5.67(2)·10$^{-10}$ |
| $m$ | 2.86(4) | 2.71(5) | 2.55(2) | 2.08(8) | 2.67(7) |
| $B_{Raman}$ / s$^{-1}$ K$^{-n}$ | 7.22(7)·10$^{-4}$ | 3.81(5)·10$^{-4}$ | 1.82(8)·10$^{-4}$ | 4.81(7)·10$^{-4}$ | 1.74(3)·10$^{-4}$ |
| $n$ | 6.36(1) | 6.43(2) | 6.75(1) | 6.83(2) | 6.47(1) |
| $\tau_{QTM}$ for $H_{dc}$ = 0 Oe / s | 0.29(5) | 0.37(3) | 1.01(2) | 1.19(1) | 1.04(3) |
| $\tau_{QTM}$ for $H_{dc}$ = 600 Oe / s | 1.06(7) | 2.30(5) | 2.99(2) | 3.11(4) | 1.71(5) |
| $\tau_0$ / s | 1.78(2)·10$^{-17}$ | 5.55(3)·10$^{-17}$ | 9.35(2)·10$^{-17}$ | 3.55(4)·10$^{-16}$ | 8.51(2)·10$^{-14}$ |
| $\Delta E$ in cm$^{-1}$ [$\Delta E / k_B$ in K] | 199.04 (fixed) [284.4] | 199.04 (fixed) [284.4] | 199.04 (fixed) [284.4] | 199.04 (fixed) [284.4] | 217.65 [313.15] |

**Comment to Fig. S6–S12 and Table S7 – fitting of *ac* magnetic data using the *relACs* program**

All field- and temperature-variable alternate-current (*ac*) magnetic characteristics were fitted using a *relACs* program (for details see Ref. S11). All *ac* magnetic characteristics (frequency dependences of out-of-phase and in-phase magnetic susceptibilities together with the related Argand plots) were simultaneously fitted using the generalized Debye model (equation S1):

$$\chi(\omega) = \chi_S + \frac{\chi_T - \chi_S}{(1 + i\omega\tau)^{1-\alpha}} \tag{S1}$$

where $\chi_S$ is the adiabatic susceptibility, $\chi_T$ is the isothermal susceptibility and $\alpha$ represents the distribution of relaxation times ($\tau$). The best-fit curves obtained within the *relACs* program are presented in Fig. S7–S12. The resulting relaxation times were plotted against the magnetic field (Fig. S7, S9, and S11) or temperature (Fig. S8, S10, S12). The whole set of dependencies for each compound was simultaneously fitted taking into account four different magnetic relaxation processes (equation S2):

$$\tau^{-1}(H,T) = A_{direct}H^m T + B_{Raman}T^n + \tau_{QTM}^{-1} + \tau_0^{-1}\exp\left(-\frac{\Delta E}{k_B T}\right) \tag{S2}$$

where the first component describes a direct process, the second one reflects Raman relaxation, the third represents quantum tunneling of magnetization effect (QTM), and the last is the Orbach thermal relaxation. In the first step of fitting, the energy barrier value of the Orbach process ($\Delta E$ = 199.04 cm$^{-1}$) was taken from the *ab initio* calculations as the energy of the first excited $m_J$ level, calculated for the iron **Dy$_2$Fe$_2$** analog (for details see Ref. S3). This process allowed for a good fit of the three-dimensional $\tau^{-1}(H,T)$ plane to the experimental data and obtain reasonable physical parameters (Table S7). Nevertheless, an alternative fit without fixing the Orbach energy barrier was also performed, using the previously obtained parameters as starting ones. Both procedures realized within the *relACs* program, using the simultaneous fitting of three curves, allowed us to obtain reasonable physical parameters. The best-fit curves, together with the course of individual relaxation processes, are shown in Fig. S7–S12. For more details regarding Ref. S3 and Ref. S11.
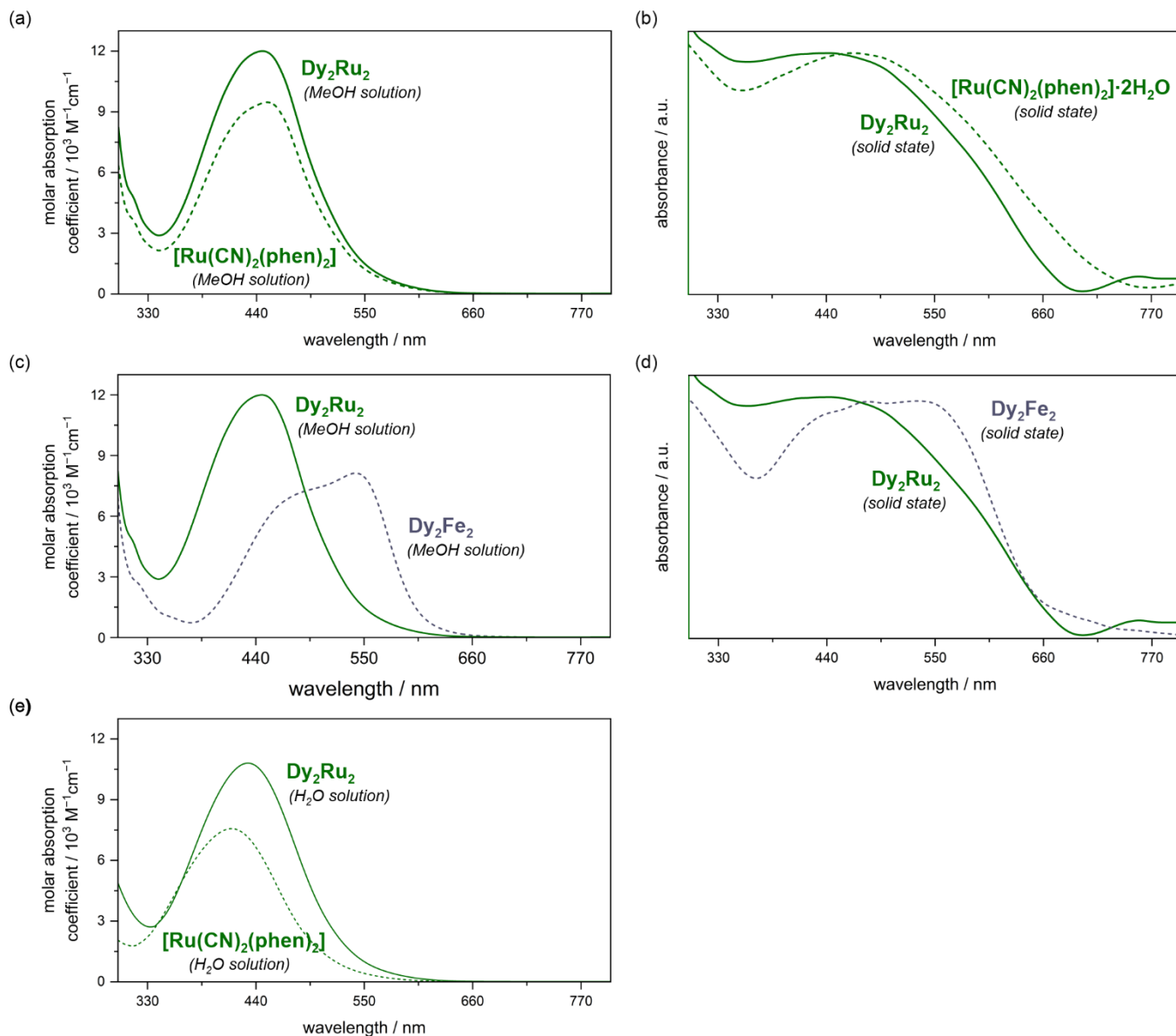
**Fig. S13** UV-vis absorption spectra of **Dy₂Ru₂** compared with the [Ru$^{II}$(CN)$_2$(phen)$_2$] precursor in the MeOH solution (a), the water solution (e) and the solid state (b), as well as the comparison of the absorption spectra of **Dy₂Ru₂** and the previously reported **Dy₂Fe₂** analog[S3] in the MeOH solution (c) and the solid state (d), all gathered in the 300–800 nm range. The observed absorption bands in the visible region correspond to the Ru(II)-to-phen charge transfer (MLCT) transitions.[S15,S16]
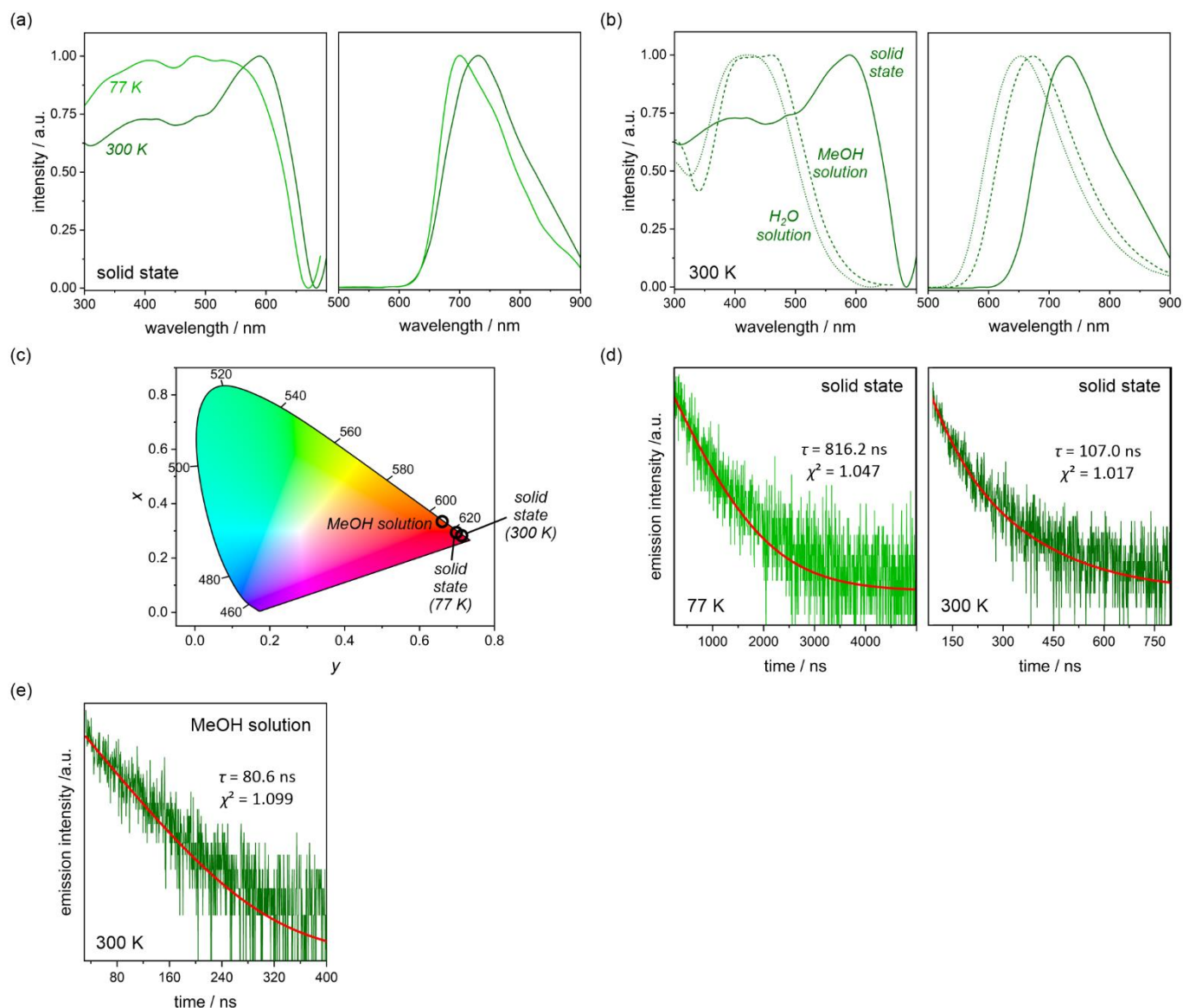
**Fig. S14** Photoluminescent properties of *cis*-[Ru$^{II}$(CN)$_2$(phen)$_2$]·2H$_2$O precursor: comparison of the solid-state excitation and emission spectra gathered at 77 K ($\lambda_{exc}$ = 400 nm, $\lambda_{em}$ = 700 nm) and 300 K ($\lambda_{exc}$ = 400 nm, $\lambda_{em}$ = 731 nm) (a), comparison of the excitation and emission spectra in the MeOH solution ($\lambda_{exc}$ = 400 nm, $\lambda_{em}$ = 673 nm), the water solution ($\lambda_{exc}$ = 400 nm, $\lambda_{em}$ = 651 nm) and the solid-state ($\lambda_{exc}$ = 400 nm, $\lambda_{em}$ = 731 nm) at 300 K (b), the corresponding emission colors in the MeOH solution and solid-state presented on the CIE 1931 chromaticity diagram (c), and the respective emission decay profiles (d–e). The related spectroscopic parameters of the emission patterns and the best-fit parameters for the emission decay profiles (red lines) are gathered in Table S8.
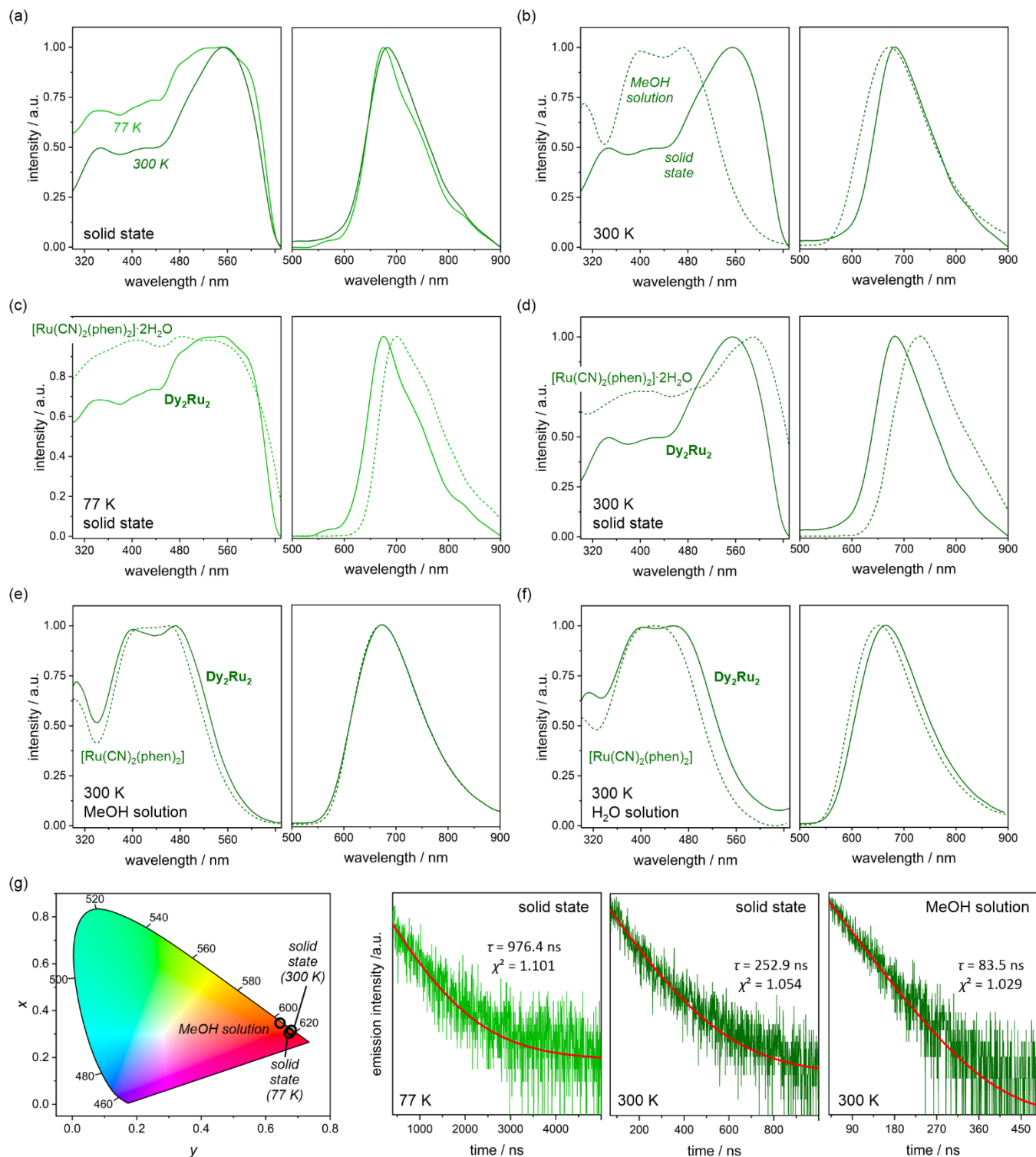
**Fig. S15** Photoluminescent properties of **Dy₂Ru₂**: comparison of the solid-state excitation and emission spectra gathered at 77 K ($\lambda_{exc}$ = 400 nm, $\lambda_{em}$ = 675 nm) and 300 K ($\lambda_{exc}$ = 400 nm, $\lambda_{em}$ = 683 nm) (a), comparison of the excitation and emission spectra in the MeOH solution ($\lambda_{exc}$ = 400 nm, $\lambda_{em}$ = 673 nm) and the solid-state ($\lambda_{exc}$ = 400 nm, $\lambda_{em}$ = 683 nm) at 300 K (b), comparison of the excitation and emission spectra of **Dy₂Ru₂** and the *cis*-[Ru$^{II}$(CN)₂(phen)₂]·2H₂O precursor in solid-state at 77 K ($\lambda_{exc}$ = 400 nm, $\lambda_{em}$ = 675 nm and 700 nm, respectively) (c), at 300 K ($\lambda_{exc}$ = 400 nm, $\lambda_{em}$ = 683 nm and 731 nm, respectively) (d), for the MeOH solution ($\lambda_{exc}$ = 400 nm, $\lambda_{em}$ = 673 nm) at 300 K (e), and the water solution ($\lambda_{exc}$ = 400 nm, $\lambda_{em}$ = 665 nm and 651 nm, respectively) at 300 K (f), the corresponding emission colors in the solution and solid-state presented on the CIE 1931 chromaticity diagram (g), and the represenative emission decay profiles (h). The related spectroscopic parameters of the emission patterns and the best-fit parameters for the emission decay profiles (red lines) are gathered in Table S8.

**Table S8** Selected spectroscopic parameters of the emission patterns and the best-fit parameters for the emission decay profiles for *cis*-[Ru$^{II}$(CN)$_2$(phen)$_2$]·2H$_2$O precursor and **Dy$_2$Ru$_2$** (see Fig. S14 and S15).

| compound | | *cis*-[Ru$^{II}$(CN)$_2$(phen)$_2$]·2H$_2$O | | | Dy$_2$Ru$_2$ | | |
|---|---|---|---|---|---|---|---|
| *T* / K | | 77 K | 300 K | | 77 K | 300 K | |
| state | | solid-state | solid-state | MeOH solution | solid-state | solid-state | MeOH solution |
| $\lambda_{em}$ / nm | | 700 | 731 | 673 | 675 | 683 | 673 |
| FWHM* / nm | | 131.29 | 151.23 | 149.50 | 116.73 | 126.01 | 150.21 |
| CIE 1931 chromaticity parameters | *x* | 0.70199 | 0.71588 | 0.66153 | 0.67441 | 0.6768 | 0.64835 |
| | *y* | 0.29392 | 0.28407 | 0.33439 | 0.32366 | 0.32122 | 0.34475 |
| emission decay profile | $\tau$ /ns | 816.2 | 107.0 | 80.6 | 976.4 | 252.9 | 83.5 |
| | $\chi^2$ | 1.047 | 1.017 | 1.099 | 1.101 | 1.054 | 1.029 |

*FWHM = full width at half maximum for the emission band

Comment on the enhancement of luminescence in **Dy₂Ru₂** when compared with the Ru(II)-cyanido precursor

We report the enhancement of luminescent properties in **Dy₂Ru₂** when compared with the Ru(II)-cyanido precursor which is depicted by the significantly higher value of QY and a much longer emission lifetime (see the main text and Table S8). It can be postulated that the increase in emission quantum yield can be related to the coordination of the $[Ru^{II}(CN)_2(phen)_2]$ metalloligands to the lanthanide ions is related to its influence not only on the emissive triplet metal-to-ligand charge transfer ($^3$MLCT) stats, changing the emission energy but also on the higher-lying MC states, which are responsible for quenching the emissive levels.

A similar effect was recently observed in the work of L. Pilia and F. Artizzu for the heterometallic d-f cyanido-bridged Ru(II)–Er(III) tetranuclear assembly,[S17] where the formation of cyanido bridges between Er(3+) ions and $[Ru^{II}(CN)_2(bpy)_2]$ complexes (analogous to the reported phen-containing ones) significantly increases the quantum efficiency of the Ru(II) luminophore. Indeed, the DFT calculations presented by the authors indicated that the stabilization effect related to the coordination of the metalloligand to Er(III) centers influences both the MLCT (or MLL'CT) as well as the MC (metal-centered but ligand-contaminated) excited states. In addition, $e_g$-like orbitals, which significantly contribute even to the LUMO+1 in Ru(II) centers, are raised in energy in the heterometallic system, resulting in an even larger energy increase in the $^3$MC states with respect to the emissive $^3$MLCT, partly suppressing the main deactivation channel of the emission. These observations for the tetranuclear Ru(II)–Er(III) system can provide a reliable explanation of the origin of the observed notable increase in the emission quantum yield in the reported **Dy₂Ru₂**.

<u>Broadened discussion on the energy shifts in absorption and luminescence spectra in **Dy₂Ru₂** when compared
with the Ru(II)-cyanido precursor in solid state and solution</u>

As we explained in the main article, the shift of the excitation and emission bands in **Dy₂Ru₂** in the solid state when compared with the precursor is related to the coordination of the cyanido ligand to the Dy$^{III}$ center (Fig. 3, Fig. S13–S15). This interaction shifts electron density on the CN$^−$ ligand and increases the metal-to-ligand $\pi$ back-donation. The highest occupied molecular orbitals of mixed Ru $d$ ($t_{2g}$) and cyanido $\pi^*$ character are therefore stabilized relative to the lowest unoccupied molecular orbitals of phen ligand $\pi^*$ character, resulting in a net destabilization of MLCT excited states. This increases the energy gap between the ground state located on Ru$^{II}$ and the MLCT excited states, which causes a blueshift of absorption and emission. Such behavior was very recently presented also for the systems containing [Ru$^{II}$(CN)$_2$(bpy)$_2$]-complexes,[S17] analogous to the phen-containing ones reported in this work, moreover, a similar coordination-driven shift emission is quite commonly observed.[S18–S22]

After dissolving the **Dy₂Ru₂** compound in a solvent of a high Lewis-acidity, such as methanol (MeOH) forming the MeOH···NC hydrogen bonds, the absorption and emission bands shift towards higher energies (ca. 10 nm) when compared with the solid-state (Fig. S13–S15). It means that supramolecular interactions for these cases shift electron density on the cyanido ligand and increase the metal-to-ligand $\pi$ back-donation, which affects the respective MLCT excited state. As a result, the emission of **Dy₂Ru₂** changes upon dissolution in MeOH from 683 to 673 nm. Such an effect of the solvent on the MLCT states is often observed for the [Fe$^{II}$/Ru$^{II}$(CN)$_2$(bpy)$_2$]-based systems and the other related Ru(II) complexes.[S3,S11,S17,S19,S23–S25]

Then, for the precursor, the analogous shift of the absorption/emission bands after dissolution also appears but it is larger (i.e., ca. 60 nm for the emission maximum). This is related to the contribution of two *cis*-oriented cyanido groups to the interaction of the complex with solvent molecules which more significantly changes the electron density distribution within the complex when both the cyanido ligands are non-coordinated to the second metal center. As a result, the dissolution-induced effect on the relative energy of the MLCT state is larger, i.e., we observe the shift from 731 to 673 nm upon the dissolution of the [Ru$^{II}$(CN)$_2$(phen)$_2$] precursor in MeOH.

This means that the emission maxima of **Dy₂Ru₂** and the [Ru$^{II}$(CN)$_2$(phen)$_2$] precursor coincidentally appear at the same wavelength. This happens because the effect of the coordination of the lanthanide ion on the MLCT states within the Ru(II) complex (shifting the energy to the higher energies) is comparable to the interaction with methanol molecules through MeOH···NC hydrogen bonds with the second cyanido ligand which is free in the [Ru$^{II}$(CN)$_2$(phen)$_2$] precursor.

To test this interpretation, we measured the luminescence properties of the **Dy₂Ru₂** and [Ru$^{II}$(CN)$_2$(phen)$_2$] in water (Fig. 3, and S13–S15), a much more Lewis-acidic solvent, which should emphasize differences between the compound and the precursor in the solution (as was demonstrated in Ref. S3, the {Dy$^{III}$$_2$(Fe/Ru)$^{II}$$_2$}$^{6+}$ molecular cations will survive also in the aqueous solution). Both of them show an expected broadband emission in water, however, compared to the methanolic solution, the emission maximum is more blue-shifted for the precursor, i.e., the emission maximum for **Dy₂Ru₂** appears at 665 nm while for the precursor at 651 nm. This means that the blueshift related to the interaction between two non-bridging cyanido ligands of the [Ru$^{II}$(CN)$_2$(phen)$_2$] precursor is stronger than the combined blueshifts, related (1) to the coordination of one of the cyanido ligands of Ru(II) complex to the lanthanide(III) center and (2) to the interaction of the remaining non-bridging cyanido ligand with the solvent, which happen in **Dy₂Ru₂**.

More importantly, this observation confirms the above-mentioned interpretation that the luminescence in methanolic solution is just coincidentally observed in the same range for the compound and the precursor. So it can be concluded that the shifts of the absorption and/or emission bands (optical chromism) in the solution of Fe/Ru(II)-polypyridyl complexes are mainly due to the influence of the solvent molecules, however, the influence of metal ion coordination introduces a rather constant shift value to the bands, unaffected by the environment in which the molecules are dispersed.[S17,S19]

## Literature

S1     E. Wachter, D. K. Heidary, B. S. Howerton, S. Parking and E. C. Glazer, *Chem. Commun.*, 2012, **48**, 9649.

S2     J. N. Demas, T. F. Turner and G. A. Crosby, *Inorg. Chem.*, 1969, **8**, 674.

S3     M. Liberka, M. Zychowicz and S. Chorazy, *Inorg. Chem. Front*., 2024, **11**, 2081.

S4     T. Neumann, M. Rams, C. Wellm and C. Nather, *Cryst. Growth Des.*, 2018, **18**, 6020.

S5     S. Chorazy, A. M. Majcher, M. Kozieł, J. Kobylarczyk, S. Ohkoshi and R. Podgajny, *Chem .Eur. J.*, 2018, **24**, 15533.

S6     G. M. Sheldrick, *TWINABS*, University of Göttingen, Germany, 2009.

S7     G. M. Sheldrick, *Acta Crystallogr. Sect. A Found. Adv*., 2015, **A71**, 3.

S8     L. J. Farrugia, *J. Appl. Crystallogr*., 2012, **45**, 849.

S9     A. Altomare, C. Cuocci, C. Giacovazzo, A. Moliterni, R. Rizzi, N. Corriero and A. Falcicchio, *J. Appl. Crystallogr.*, 2013, **46**, 1231.

S10   M. Liberka, J. J. Zakrzewski, M. Heczko, M. Reczynki, S. Ohkoshi and S. Chorazy, *Inorg. Chem.*, 2021, **60***, 4093.

S11   M. Liberka, M. Zychowicz, W. Zychowicz and S. Chorazy, *Chem. Commun.*, 2022, **58**, 6381.

S12   S. Chorazy, J. J. Zakrzewski, J. Wang, S. Ohkoshi, B. Sieklucka, *CrystEngComm*, 2018, **20**, 5695.

S13   M. Llunell, D. Casanova, J. Cirera, J. Bofill, P. Alemany, S. Alvarez, M. Pinsky and D. Avnir, SHAPE v. 2.1.; University of Barcelona: Barcelona, Spain, 2013.

S14   D. Casanova, J. Cirera, M. Llunell, P. Alemany, D. Avnir and S. Alvarez*, J. Am. Chem. Soc*., 2004, **126**, 1755.

S15   L. Fodor, G. Lendvay and A. Horvath, *J. Phys. Chem. A*, 2007, **111**, 12891.

S16   Y. Hou, P. Xie, K. Wu, J. Wang, B. Zhang and Y. Cao, *Sol. Energy Mater. Sol. Cells*, 2001, **70**, 131.

S17   D. Mara, Z. Cai, S. Bonabello, S. Penna, R. Van Deun, P. Deplano, L. Marchio, L. Pilla and F. Artizzu, *Cryst. Growth Des*., 2024, **24**, 3798.

S18   L. Schmid, C. Kerzig, A. Prescimone and O. S. Wenger, *JACS Au*, 2021, **1**, 819.

S19   F. Artizzu, L. Pilia, A. Serpe, D. Mara, M. F. Casula, L. Marchio and P. Deplano, *Molecules*, 2023, **28**, 2871.

S20   A. Schmidt, M. Hollering, J. Han, A. Casini and F. E. Kühn, *Dalton Trans*., 2016, **45**, 12297.

S21   S. Evariste, A. M. Khalil, M. E. Moussa, A. K.-W. Chan, E. Y.-H. Hong, H.-L. Wong, B. Le Guennic, G. Calvez, K. Costuas, V. W.-W. Yam and C. Lescop, *J. Am. Chem. Soc*. 2018, **140**, 12521.

S22   J.-Q. Liu, Z.-D. Luo, Y. Pan, A. K. Singh, M. Trivedi and A. Kumar, *Coord. Chem. Rev*., 2020, **406**, 213145.

S23   N. Karaoun and A. K. Renfrew, *Chem. Commun.,* 2015, **51**, 14038.

S24   J. Shum, P. Kam-Keung Leung and K. Kam-Wing. Lo, *Inorg. Chem.,* 2019, **58**, 2231.

S25   E. Wachter, D. K. Heidary, B. S. Howerton, S. Parkin and E. C. Glazer, *Chem. Commun*., 2012, **48**, 9649.